Numerical study of turbulent flow fields in urban areas using modified $k-\varepsilon$ model and large eddy simulation

Takeshi Ishihara [a], Guo-Wei Qian [a,*], Yi-Hong Qi [b]

[a] Department of Civil Engineering, School of Engineering, The University of Tokyo, Tokyo, Japan
[b] Department of Civil Engineering, Yango University, Fuzhou, Fujian, China

A B S T R A C T

In this study, a numerical urban model is proposed, which includes digital elevation model for topography, land-use database, digital maps on buildings and vegetation. Turbulent flow fields in the cube arrays with different packing densities and a real urban area are investigated by both modified $k-\varepsilon$ model and large eddy simulation (LES). It is found that the simulation with the modified $k-\varepsilon$ model is less sensitive with grid resolution and is able to predict turbulent flow fields over uniform urban-like cube arrays, where the turbulent flow fields are fully developed. However, the modified $k-\varepsilon$ model shows some discrepancies between the predicted and measured turbulent flow fields in the urban area, where the flow fields are strongly affected by the organized motions generated by surrounding buildings. The LES model is able to predict turbulent flow fields in the uniform urban-like cube arrays as well as in the non-uniform urban area. The accuracy of LES model strongly affected by the grid resolution and a grid dependency study is conducted in the target area.

1. Introduction

Amenity, security and convenience are highly valued in modern city, however, they are usually endangered by strong wind. Firstly, wind environment is getting worse due to strong wind around high rise buildings (Simiu and Scanlan, 1996). In the design stage, the effects from the high rise building to be built on the wind environment around this building will be evaluated, and mitigation measures, such as tree will be applied. Thus, a generalized and convenient wind prediction model with high accuracy is required to predict the wind climate in the urban area, including buildings and trees. Secondly, strong wind can result in a lot of damages when typhoon attacks (Kawaguchi, 2000). For example, the cladding of buildings can be damaged by the local maximum wind speed, and falling materials will then bring further damages to a wide area. It is important, in opinion of risk management, to carry out prediction in a wide area on damages due to strong wind. Additionally, strong wind can strongly affect the use of infrastructures. Typhoon Maemi (Typhoon 0314) attacked Miyakojima island in Okinawa prefecture in 2003 and resulted in the collapse of more than 1000 utility poles, which strongly affected the daily life of local people and reconstruction (Ishihara et al., 2005b). Moreover, strong wind can also damage the convenience of the transportation system in urban areas. Particularly, the train service

delays or stops due to strong wind not only bring inconvenience to citizens but also result in huge economic losses. Although some measures, such as windbreak fence, have been studied, it is essential to identify the strong wind areas along railway lines. A method to predict wind climate with high resolution along the railway is required because it is very long in the longitudinal direction and very short in the lateral direction as shown by Misu and Ishihara (2018).

A prediction method for the wind field in the urban area was achieved by conducting wind tunnel tests (Ishihara et al., 2005a). Many efforts have also been applied using numerical simulations with the development of the computer science (Kanda, 2006; Nozu et al., 2008; Yoshie et al., 2011; He et al., 2018; Giometto et al., 2017; Qi and Ishihara, 2018), which are classified by the modeling on the surface roughness as well as the turbulence model.

Three approaches are used to model the surface roughness in urban areas. The first is the roughness length model, which was applied by Grimmond and Oke (1999), Xian et al. (2002), Blocken et al. (2007) and Varquez et al. (2015). It assumes that the mean wind speed profile follows the logarithmic law near the ground and use the roughness length to describe the local surface roughness. However, this model cannot accurately represent the effects of buildings and vegetation in a micro scale wind environment. The second is called the rigid wall approach, which

---

* Corresponding author.
  E-mail address: qian@bridge.t.u-tokyo.ac.jp (G.-W. Qian).

was applied by Coceal et al. (2006), Gousseau et al. (2011), Blocken et al. (2012), Philips et al. (2013), Cheng and Porté-Agel (2015) and Antoniou et al. (2017). It explicitly describes the detailed geometry of each building and uses fine grids close to the surface of buildings to catch the small vortex near the boundary of buildings, therefore it provides possibility to predict the flow fields around buildings with high accuracy. However, it requires a large calculation effort and its application is therefore limited in a small area. Moreover, this approach cannot model vegetation. The last approach is the canopy model, which was applied by Lien et al. (2004), Ashie et al. (2007), Enoki et al. (2009), Aumond et al. (2013), Park et al. (2014), Gutierrez et al. (2015), Qi and Ishihara (2018). It considers the force acting on the fluid, turbulence generation and dissipation due to obstacles by introducing source terms in the momentum equation and turbulence transportation equations. It requires less computational grid than that in the rigid wall approach and can be used for wind prediction in a wide area. The detailed information of buildings and trees makes it more accurate than the roughness length model. One important issue of using the canopy model is how to model surface roughness in urban areas by an available database.

Many organizations, such as the Ministry of Land, Infrastructure, Transport and Tourism of Japan (MLIT), provide a land-use database, which categorizes all surface roughness and use the roughness length z_0 to describe the extent of each roughness condition on the local wind profiles. Gutiérrez et al. (2015) estimated the packing density of buildings in the New York by land-use tax-lot output data. These packing densities were then used to evaluate the drag force coefficient. However, this indirect information can induce errors on evaluation of distribution of buildings, thus it is difficult to predict the wind field in other urban area. Kanda et al. (2013) applied a three-dimensional digital map of buildings, which provides detailed geometry information of buildings, but expensive. A comprehensive digital urban model, which includes the digital elevation model for topography and digital maps for buildings and vegetation, has not been achieved yet. The digital elevation model (DEM) is a 3D computer graphic representation of a terrain's surface created from a terrain's elevation data.

The turbulence model is also a key factor in numerical simulations on prediction of turbulent flow fields in urban areas. The first category is based on Reynolds averaged Navier-Stokes model (RANS model), which has been widely used in the engineering applications, such as Mochida et al. (2006), Enoki et al. (2009) and He et al. (2018). A number of approaches have been successfully developed in the context of modified k-ε models for the study of atmospheric boundary layer in urban context (Yang and Zhang, 2009; Parente et al., 2011; Longo et al., 2017). However, due to the deficiency of simulating unsteady phenomenon, such as vortex shedding, the RANS model may fail to predict the flow field in the wake region of buildings and trees (Rodi, 1997; Yoshie et al., 2007, 2011; Qi and Ishihara, 2018). The second category is based on LES turbulence model and has been widely used in scientific studies: Yang et al. (2006), Bailey and Stoll (2013), Mueller et al. (2014), Giometto et al. (2017), Qi and Ishihara (2018). However, few researches utilized the LES turbulence model to predict the turbulent flow field in a real urban area.

This study aims to investigate the turbulent flow fields in urban areas by using modified $k - \varepsilon$ model and LES model, and to quantitatively evaluate the accuracy of these models. In section 2, numerical methods, including governing equations, turbulence models, boundary condition and solution schemes are described. In section 3, a digital urban model is developed, including a digital elevation model for topography, a land-use database, digital maps on buildings and vegetation. The simulated turbulent flow fields over the urban-like cube arrays with different packing densities and a real urban area are compared with measurement data and evaluated by the validation metrics in section 4 and 5. Finally, conclusions are summarized in section 6.

2. Numerical model

The canopy model and turbulence models used in this study are introduced in sections 2.1. Section 2.2 describes the setup for numerical scheme and boundary condition in the numerical simulation. Validation metrics is finally explained in section 2.3.

2.1. Fluid force and turbulence models

The definition of canopy layer is the assemblage of obstacles near the ground like buildings and trees and spaces between them. Canopy model, in contrast to the rigid wall approach, introduces a source term $f_{\bar{u},i}$ to model the effects of obstacles as an external fluid force reacting on the fluid. The generalized canopy model derived by Enoki et al. (2009) is applied in this study and the fluid force in the momentum equations is shown as:

$$f_{\bar{u},i} = -\frac{F_{\bar{u},i}}{V_{grid}} = -\frac{1}{2}\rho C_f \frac{\gamma_0}{l_0}|\bar{u}|\bar{u}_i \tag{1}$$

where, $f_{\bar{u},i}$ is the fluid force in the volume of grid, V_{grid}. $|\bar{u}|$ is the absolute value of mean wind speed per unit volume, C_f is the equivalent drag coefficient, l_0 is defined as the representative length scale of obstacles and γ_0 is the packing density. The calculations of canopy parameters for vegetation and buildings are explained in section 3.

In order to close the governing equations on continuity and momentum conservation, Reynolds stress τ_{ij} is normally modelled following the eddy viscosity hypothesis, where τ_{ij} are assumed as product of the fluid strain and an eddy viscosity.

$$\tau_{ij} = 2\mu_t \bar{S}_{ij} + \frac{\delta_{ij}}{3}\tau_{kk}, \quad \bar{S}_{ij} = \frac{1}{2}\left(\frac{\partial \bar{u}_i}{\partial x_j} + \frac{\partial \bar{u}_j}{\partial x_i}\right) \tag{2}$$

Here, δ_{ij} is the Kronecker delta function, which is 1 if i and j are equal, and 0 otherwise. $\bar{S}_{ij}$ is the strain rate tensor. μ_t is the eddy viscosity and is defined as:

$$\mu_t = \rho C_\mu \frac{\bar{k}^2}{\bar{\varepsilon}} \tag{3}$$

where constant C_μ is 0.09, $\bar{k}$ and $\bar{\varepsilon}$ are the turbulent kinetic energy and the dissipation of turbulent kinetic energy respectively. The term $(\delta_{ij}/3)\tau_{kk}$ is absorbed into the pressure term (Bechmann and Sørensen, 2010). $\bar{k}$ and $\bar{\varepsilon}$ are obtained by solving two additional equations. In the simulation with the modified $k - \varepsilon$ model, the standard $k - \varepsilon$ model with Kato-Launder modification is selected. $\bar{k}$ and $\bar{\varepsilon}$ are calculated by:

$$\frac{\partial(\rho\bar{k})}{\partial t} + \frac{\partial(\rho\bar{k}\bar{u}_i)}{\partial x_i} = \frac{\partial}{\partial x_j}\left[\left(\mu + \frac{\mu_t}{\sigma_k}\right)\frac{\partial\bar{k}}{\partial x_j}\right] - \left(\frac{2}{3}\rho\bar{k}\delta_{ij}\frac{\partial\bar{u}_i}{\partial x_j} - P_k\right) - \rho\bar{\varepsilon} + f_k \tag{4}$$

$$\frac{\partial(\rho\bar{\varepsilon})}{\partial t} + \frac{\partial(\rho\bar{\varepsilon}\bar{u}_i)}{\partial x_i} = \frac{\partial}{\partial x_j}\left[\left(\mu + \frac{\mu_t}{\sigma_\varepsilon}\right)\frac{\partial\bar{\varepsilon}}{\partial x_j}\right] - C_{1\varepsilon}\frac{\bar{\varepsilon}}{\bar{k}}\left(\frac{2}{3}\rho\bar{k}\delta_{ij}\frac{\partial\bar{u}_i}{\partial x_j} - P_k\right) - C_{2\varepsilon}\rho\frac{\bar{\varepsilon}^2}{\bar{k}} + f_\varepsilon \tag{5}$$

where $C_{1\varepsilon} = 1.44$, $C_{2\varepsilon} = 1.92$, $\sigma_k = 1.0$ and $\sigma_\varepsilon = 1.3$ are the constants. For incurring overestimation of turbulent kinetic energy at the stagnation point, the turbulence source term P_k is estimated by Kato (1993). The source terms in $\bar{k}$ and $\bar{\varepsilon}$ equations are introduced to consider the promoting process of energy cascade in the canopy layer. Specifically, f_k is to model the turbulent kinetic energy generated by the existence of canopy and the accelerated cascade of turbulent kinetic energy from large scale to small scales caused by vegetation as well. Accordingly, f_ε should also be incorporated into ε equation to consider the increase as well as reduction in the dissipation rate due to the generation and reduction in k equation, respectively.

$$f_k = \frac{1}{2}\beta_p \rho C_f \frac{\gamma_0}{l_0}|\bar{u}|^3 - \frac{1}{2}\beta_d \rho C_f \frac{\gamma_0}{l_0}|\bar{u}|\bar{k} \tag{6}$$

$$f_\varepsilon = \frac{1}{2}C_{p\varepsilon 1}\beta_p\rho\frac{\overline{\varepsilon}}{\overline{k}}C_f\frac{\gamma_0}{l_0}|\overline{u}|^3 - \frac{1}{2}C_{p\varepsilon 2}\beta_d\rho C_f\frac{\gamma_0}{l_0}|\overline{u}|\overline{\varepsilon} \qquad (7)$$

where the model constants β_p and $C_{p\varepsilon 1}$ are set to 1.0 and 1.5, respectively, following the study by Liu et al. (1996), and Green (1992). Based on the assumption that the generation and dissipation of turbulence is cancelled out in the high packing density region, the expression of β_d and $C_{p\varepsilon 2}$ are determined as of the packing density γ_0 as shown in Equations (8) and (9), in which the parameters are identified through a series of numerical investigation by Enoki et al. (2009).

$$\beta_d = min\left[4.0, \alpha_{k1}exp\left(\frac{1-\gamma_0}{\gamma_0}\right) + \alpha_{k2}\right] \qquad (8)$$

$$C_{p\varepsilon 2} = \begin{cases} 0.7 & , \gamma_0 \leq \gamma_c \\ \alpha_{\varepsilon 1}\sqrt{sin\left[\pi\frac{\gamma_0 - \gamma_c}{2(1-\gamma_c)}\right]} + \alpha_{\varepsilon 2} & , \gamma_0 > \gamma_c \end{cases} \qquad (9)$$

where the coefficients are identified to be $\alpha_{k1} = 0.5$, $\alpha_{k2} = -0.5$, $\alpha_{\varepsilon 1} = 0.8$, $\alpha_{\varepsilon 2} = 0.7$ and $\gamma_c = 0.312$.

In LES turbulence model, the subgrid-scale Reynolds stress τ_{ij} is modelled as:

$$\tau_{ij} = -2\mu_t\overline{S}_{ij} + \frac{1}{3}\tau_{kk}\delta_{ij} \qquad (10)$$

where μ_t denotes the subgrid-scale turbulent viscosity and modelled by Smagorinsky-Lilly model (Smagorinsky, 1963), and $\overline{S}_{ij}$ is the rate-of-strain tensor for the resolved scale.

$$\mu_t = \rho L_s^2|\overline{S}| = \rho L_s\sqrt{2\overline{S}_{ij}\overline{S}_{ij}} \qquad (11)$$

where L_s is the mixing length for subgrid-scales, and defined as:

$$L_s = min\left(\kappa d, C_s V^{\frac{1}{3}}\right) \qquad (12)$$

where $\kappa = 0.42$ is the von Karman constant. d is the distance to the closest wall and V is the volume of a computational grid. C_s is Smagorinsky constant and in this study $C_s = 0.032$ is chosen based on Oka and Ishihara (2009).

2.2. Numerical scheme and boundary condition

Numerical schemes shown in Table 1 are used for simulations with the modified $k - \varepsilon$ model and the LES turbulence model. Only the $k-\varepsilon$

Table 1
Description of numerical schemes.

Items	Schemes
Spatial discretization	CDS (central differencing scheme)
Time discretization	2nd order implicit scheme
Pressure-velocity coupling	SIMPLE

Table 2
Description of boundary conditions.

Locations	Boundary conditions
Outlet Boundary	Pressure outlet
Side Boundary	Symmetry
Top Boundary	Symmetry
Bottom Boundary	Logarithmic law

model adopts QUICK for the spatial discretization. The Navier-Stokes equations are solved with the commercial CFD code ANSYS Fluent 16.2 (2015).

Boundary conditions used in simulations with the modified $k - \varepsilon$ model and the LES model are shown in Table 2. The inlet boundary condition in the simulation with the LES turbulence model is a uniform flow, and turbulent inflow is generated by the blocks for the urban-like cube arrays and spires for the real urban area. On the other hand, the measured mean wind speed and turbulence are directly used as the inlet boundary conditions for the modified $k - \varepsilon$ model.

For the $k - \varepsilon$ model, provided that the mesh cannot resolve the laminar sublayer, the centroid of the wall-adjacent cells is assumed to fall within the logarithmic region of the boundary layer, and then the law-of-the-wall is employed:

$$\frac{\overline{u}}{u_*} = \frac{1}{\kappa}ln\left(E\frac{\rho u_*z}{\mu}\right) - \Delta B \qquad (13)$$

where $\overline{u}$ is the resolved velocity tangential to the wall, z is the distance between the center of the cell and the wall, $u_* = C_\mu^{1/4}k^{1/2}$ is the friction velocity, and the constant E is 9.793. ΔB accounts for the displacement caused by the rough wall.

The logarithmic law as shown in Eq. (14) is widely used as the boundary condition for the atmospheric boundary layers (Grimmond and Oke, 1999; Xian et al., 2002; Blocken et al., 2007).

$$\frac{\overline{u}}{u_*} = \frac{1}{\kappa}ln\left(\frac{z}{z_0}\right) \qquad (14)$$

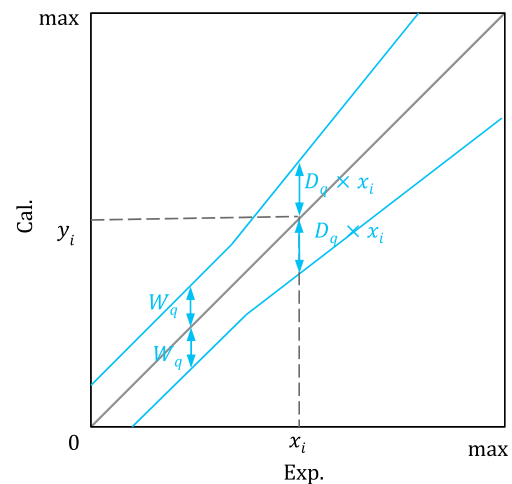where z_0 is the roughness length and defined as the height above the

Fig. 1. Schematic of Validation Metrics. The lines in blue mark the boundaries defined by q. (For interpretation of the references to colour in this figure legend, the reader is referred to the Web version of this article.)
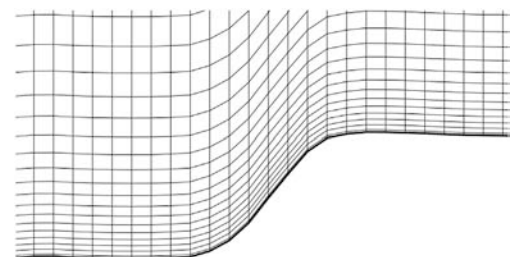

Fig. 2. The σ grid system for the digital elevation model.

Table 3
Land-use categories and corresponding roughness length. ○ denotes that canopy parameters are applied and – means that roughness length model shall be used instead of canopy model.

Number	Category	Roughness length model	Canopy model	
		z_0 (m)	z_0^* (m)	Canopy parameters
1	Rice field	0.01	0.01	–
2	Other agricultural field	0.03	0.03	–
3	Forest	0.8	0.01	○
4	Barren land	0.01	0.01	–
5	Buildings	1.0	0.01	○
6	Main traffic area	0.03	0.03	–
7	Other area	0.01	0.01	–
8	Lakes and ponds	0.0002	0.0002	–
9	Beach	0.01	0.01	–
10	Sea	0.0002	0.0002	–
11	Golf course	0.01	0.01	–

Table 4
Description of digital map on buildings.

Information	Type	Description
Position and shape	Polygon	Coordinates
Attribute	Integer	Number of floors

ground at which the mean velocity is 0. ΔB can be calculated by substituting Eq. (13) into Eq. (14).

$$\Delta B = \frac{1}{\kappa} ln \left(E \frac{\rho u_* z_0}{\mu} \right) \tag{15}$$

It should be noted that, for the $k - \varepsilon$ model used in ANSYS Fluent, the law of the wall for mean velocity are based on the non-dimensional distance from the wall, $y^* = \rho u_* z / \mu$, rather than $y^+ = \rho u_\tau z / \mu$, where $u_\tau = (\tau_w / \rho)^{1/2}$ with τ_w defined as the wall shear stress. In this study, the smallest y^* values achieved in the simulations are kept in the order of $y^* \sim 15$, which meets the requirement that the above described logarithmic law is employed only when $y^* > 11.225$ (Fluent 16.2, 2015).

While in the case of LES, the standard blended log-law type wall function is utilized by default in ANSYS Fluent as follows. When the mesh is fine enough to resolve the laminar sublayer, the wall shear stress is obtained from the laminar stress-strain relationship:

$$\frac{\overline{u}}{u_\tau} = \frac{\rho u_\tau z}{\mu} \tag{16}$$

If the mesh is too coarse that the centroid of the wall-adjacent cell falls within the logarithmic region, the law-of-the-wall is employed:

$$\frac{\overline{u}}{u_\tau} = \frac{1}{\kappa} ln \left(E \frac{\rho u_\tau z}{\mu} \right) \tag{17}$$

If the mesh is such that the first near-wall point is within the buffer region, then the two above laws are blended in accordance with a function suggested by Kader (1981). This blend of the linear and logarithmic laws of the wall is applicable for the whole range of y^+ below 300, and there are no additional stability and accuracy problems in applying it across the buffer layer as well. The averaged y^+ values in the LES simulations are achieved in a moderate order of $y^+ \sim 10$, which follows the recommendation by the Theory Guide (Fluent 16.2, 2015).
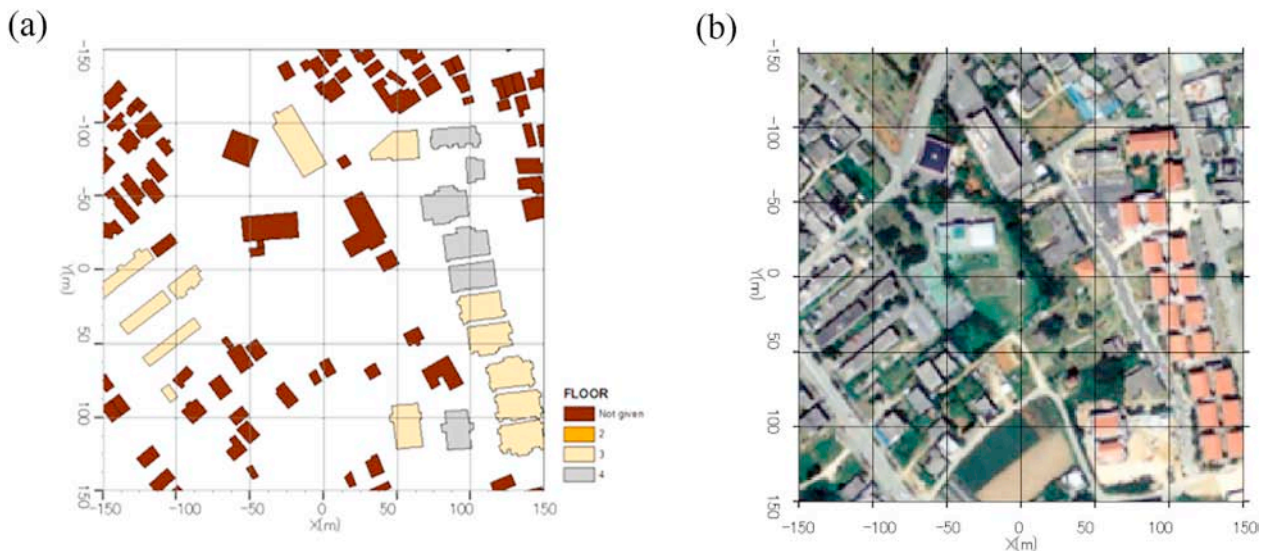

Fig. 3. Distribution of buildings around the meteorological station in Miyakojima island: (a) Digital map on buildings extracted from Zmap-TOWNII and (b) Satellite photograph by Google Earth.
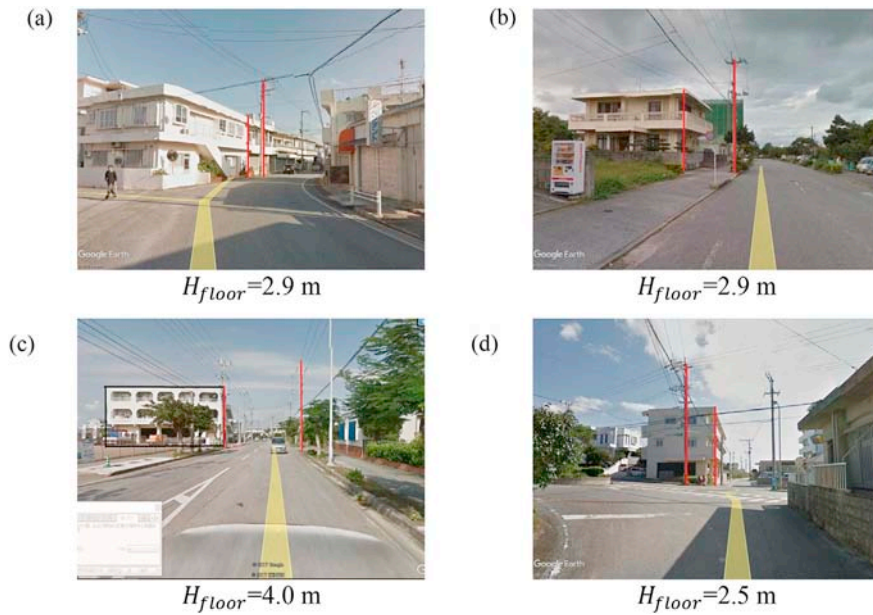
Fig. 4. Photographical measurement by Street View for buildings and the measured floor height in different locations in Miyakojima island: (a) and (b) are examples for buildings with 2 floors, (c) and (d) are samples for those with 3 floors. The height of utility pole is used as the reference value.

Table 5
Description of digital map on vegetation.

Information	Data type	Description
Position and shape	Polygon	Coordinates
Attribute	Integer	Type of vegetation

2.3. Validation metrics

In order to quantify the agreement between computational and experimental results, validation metrics, hit rate q (Schatzmann et al., 2010) is used in this study. The definition of q is given in Eq. (18) and the boundary of accurate region is shown schematically in Fig. 1.

$$q = \frac{1}{N} \sum_{i=1}^{N} n_i \, with \, n_i = \begin{cases} 1 & \left| \frac{y_i - x_i}{x_i} \right| \le D_q \quad or \quad |y_i - x_i| \le W_q \\ 0 & else \end{cases} \quad (18)$$

where, y_i and x_i are the observed (measured) and predicted (computed) values of a given variable for sample i, respectively, and N is the number of data points. The ideal values of the metrics that correspond to perfect agreement are 1.0 for q. The thresholds for q are $D_q = 0.15$ for mean wind speed and $D_q = 0.3$ for Reynolds stress since the squared variable gives error as twice as the variable itself. $W_q = 0.05|max|$ is used for both mean wind speed and Reynolds stress, in which $|max|$ is a maximum value supposed in the observation and the prediction as shown in Fig. 1.
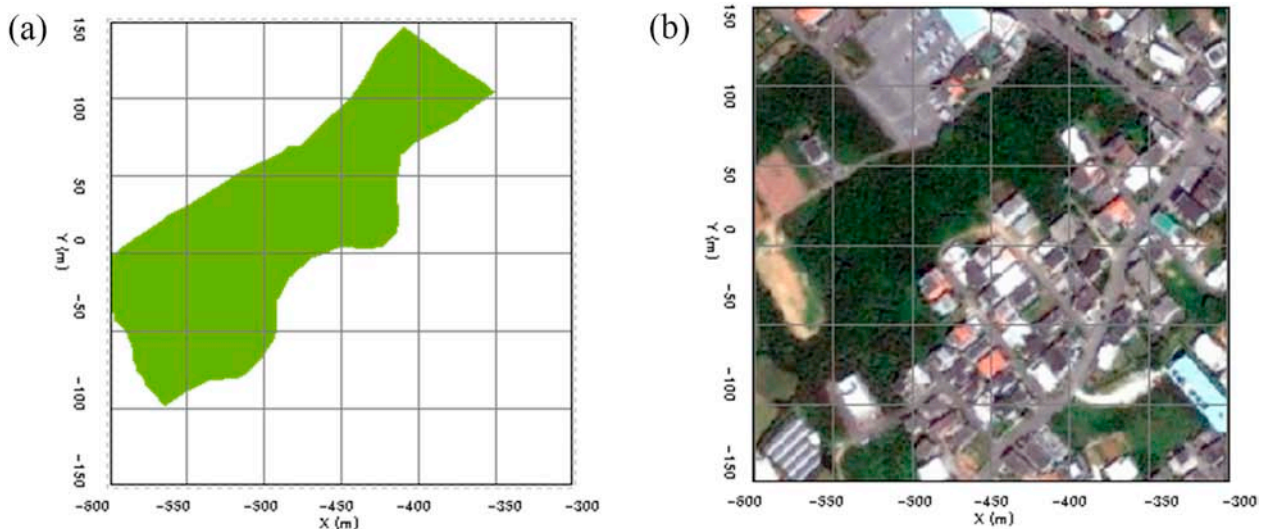

Fig. 5. Distribution of forests near the meteorological station in Miyakojima island: (a) Digital map on vegetation extracted from NEI-GIS and (b) Satellite photograph by Google Earth.
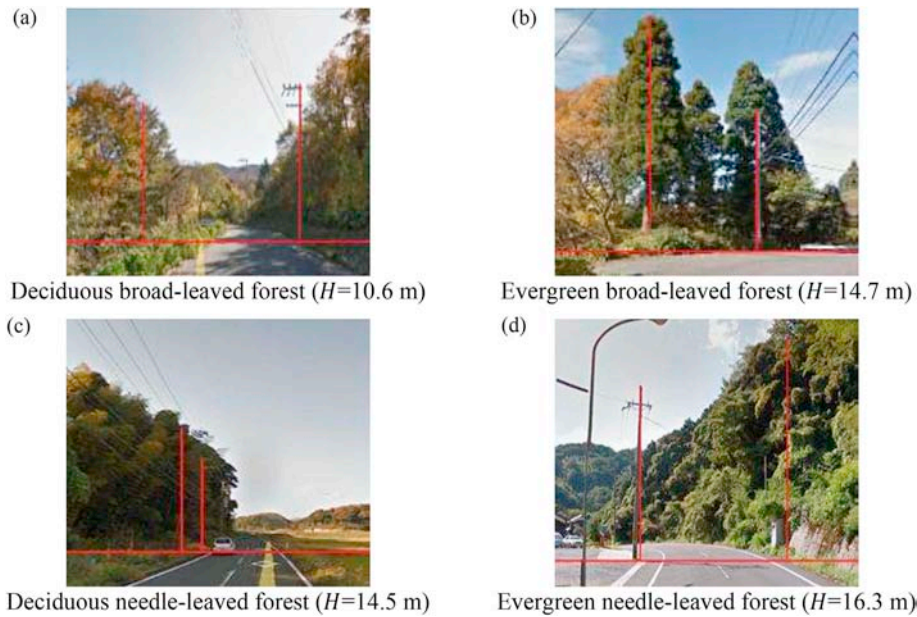
(a) Deciduous broad-leaved forest (*H*=10.6 m)

(b) Evergreen broad-leaved forest (*H*=14.7 m)

(c) Deciduous needle-leaved forest (*H*=14.5 m)

(d) Evergreen needle-leaved forest (*H*=16.3 m)

Fig. 6. Photographical measurement by Street View for different types of forest. The height of utility pole is used as the reference value. The average heights for (a) deciduous broad-leaved forest, (b) evergreen broad-leaved forest, (c) deciduous needle-leaved forest, and (d) evergreen needle-leaved forest are 10.6 m, 14.7 m, 14.5 m, 16.3 m, respectively.
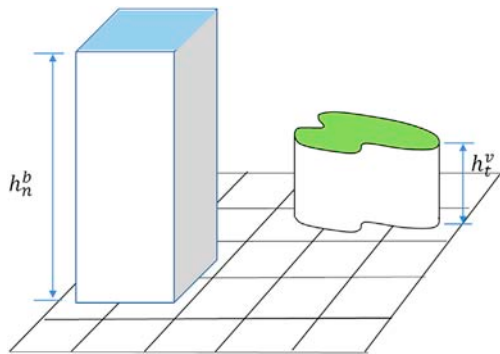
Fig. 7. Modelling of building and vegetation from the digital maps.

3. Digital urban model

To develop a digital urban model, the databases to describe the surface roughness are significant and three representative available ones are summarized below. The first is the aviation laser database by PAR-EA-LiDAR obtained by laser scan measurements, which provides high-density, high-accuracy 3D spatial data for buildings. The horizontal and vertical resolutions are 30 cm and 15 cm, respectively. However, it is high cost and only available in major cities. The second is the digital surface model (DSM) with horizontal resolution of approximately 30 m by Advanced Land Observing Satellite. Though it is available in global areas, the shapes of buildings are estimated with large errors and the heights of vegetation cannot be well captured as mentioned by Ito and Ishihara (2018). The third is the digital maps on buildings and vegetation, which contains the information of shape in vector format, the number of floors for buildings and the type for vegetation.

In section 3.1, the digital elevation model and land-use database are explained at first. The digital maps on buildings and vegetation are then
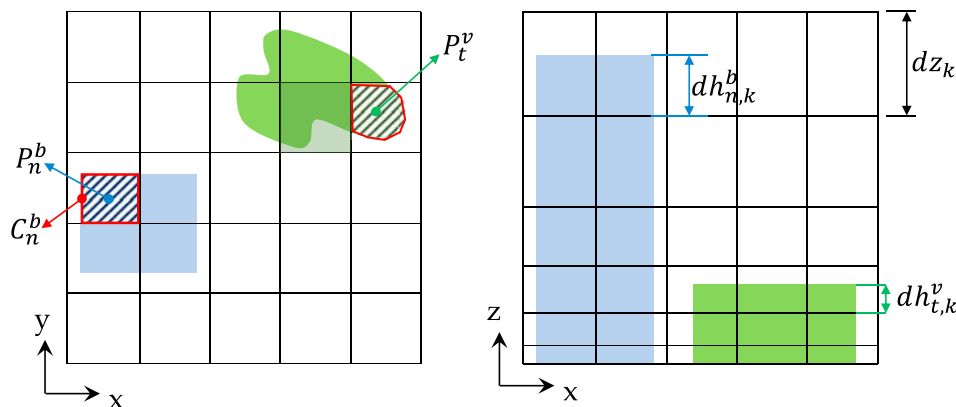

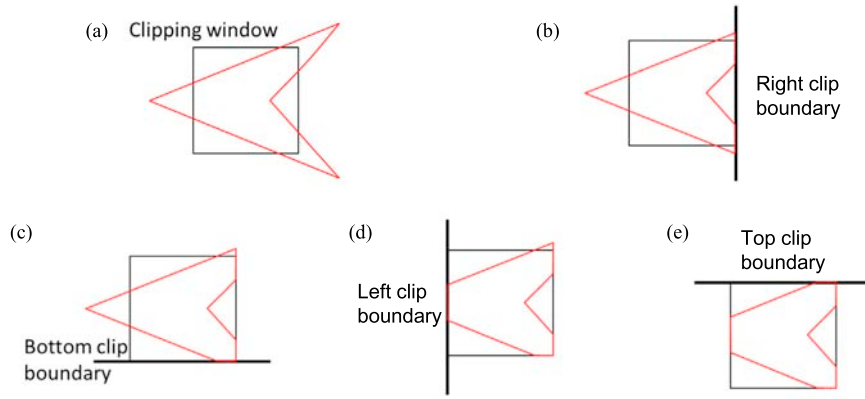**Fig. 8.** Horizontal occupied area, perimeter and effective height in computational cells.

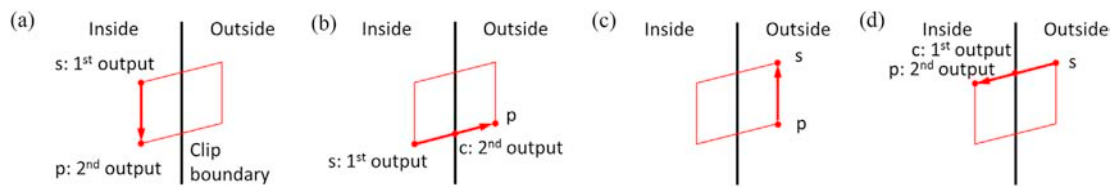**Fig. 9.** Clipping of building shape with the computational cell.

Fig. 10. Description of Sutherland and Hodgman method: (a) Case1, (b) Case 2, (c) Case 3 and (d) Case 4.
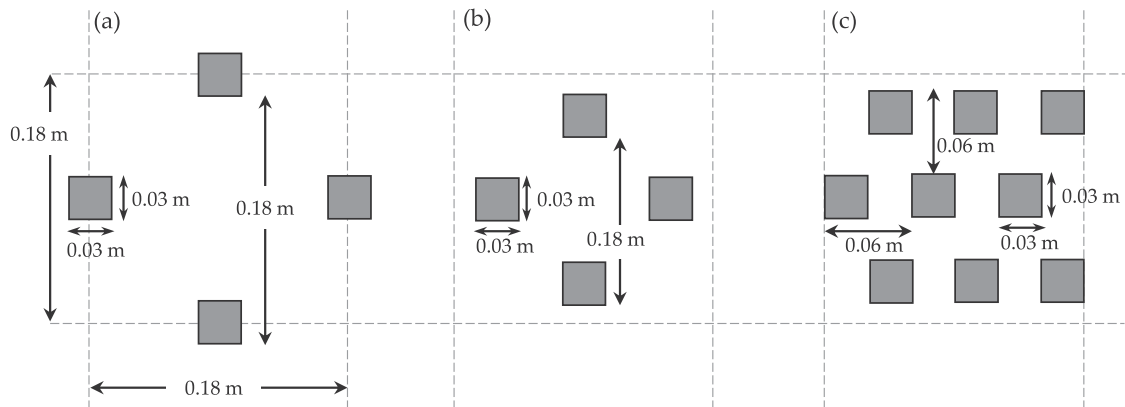

Fig. 11. Layouts of the staggered cube arrays with different packing densities: (a) $\gamma_0 = 5.6\%$, (b) $\gamma_0 = 12.4\%$ and (c) $\gamma_0 = 25\%$.
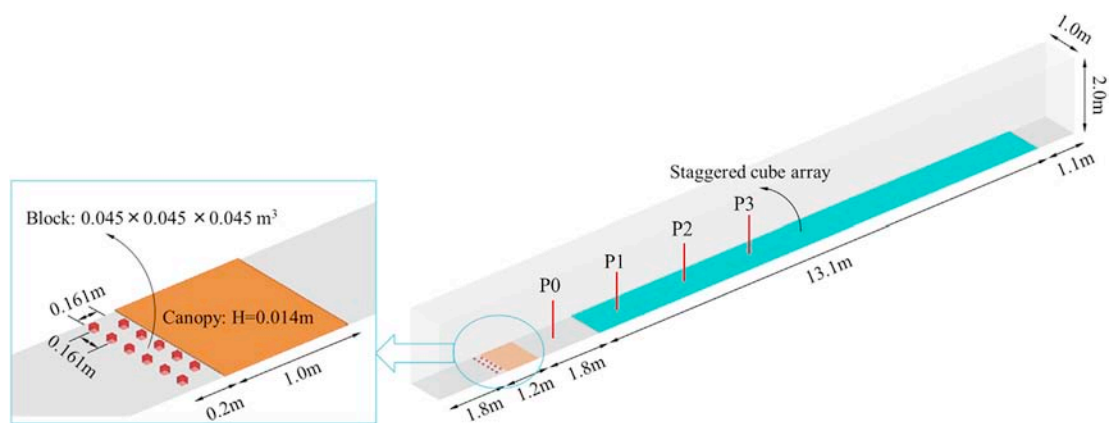

Fig. 12. Configuration of the numerical wind tunnel for simulations of staggered cube array with LES turbulence model.

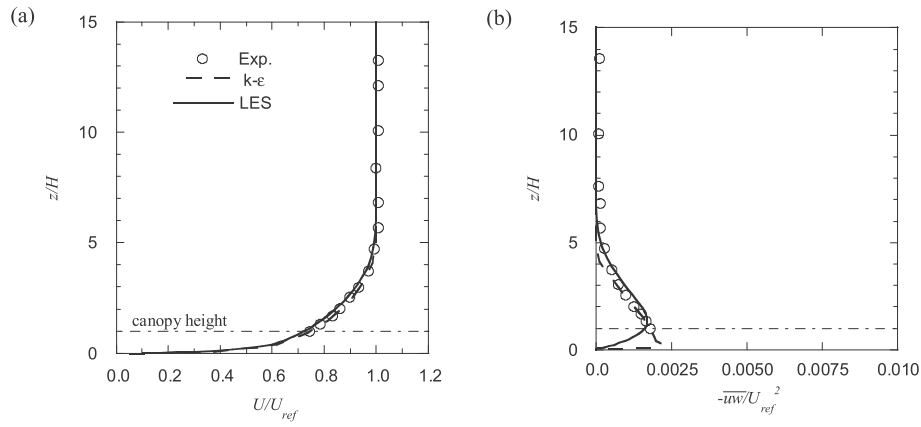**Fig. 13.** Vertical profiles of (a) normalized mean wind speed and (b) normalized Reynolds stress at the position P0 for the staggered cube arrays.
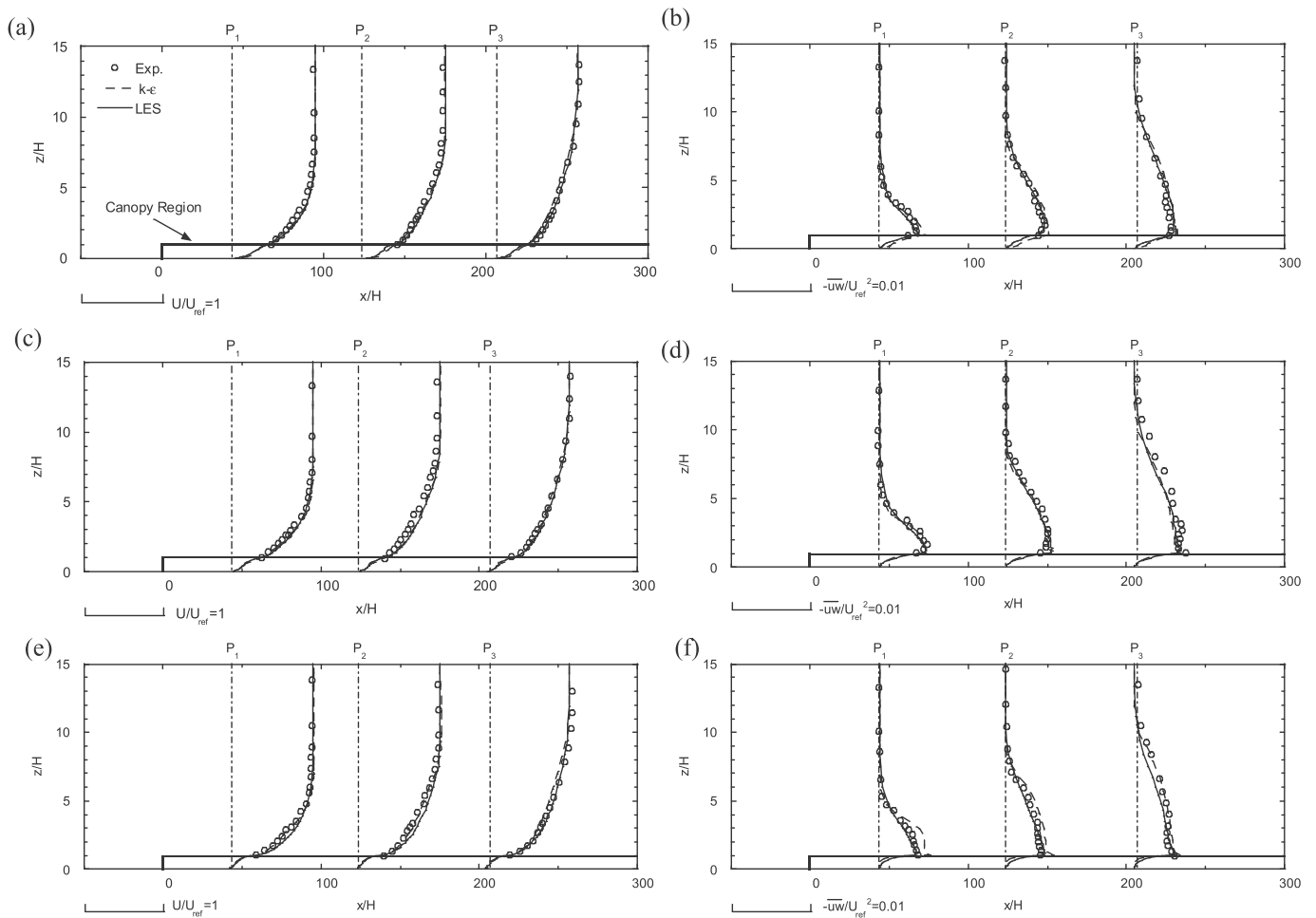

Fig. 14. Vertical profiles of normalized mean wind speed and normalized Reynolds stress on the staggered cubic array: (a), (b) $\gamma_0 = 5.6\%$, (c), (d) $\gamma_0 = 12.5\%$, (e), (f) $\gamma_0 = 25\%$.

described and the identification of height for buildings and vegetation is discussed in section 3.2. The method to calculate canopy parameters from the digital maps of buildings and vegetation is presented in sections 3.3 and 3.4. Finally, the formulation of fluid force in the mixed land use condition is proposed in section 3.5.

3.1. Digital elevation model and land-use database

The digital elevation model (DEM) is provided by Geospatial Information Authority of Japan in raster format, which describes the topography in Japan. The available minimum resolution is 10m × 10 m that is
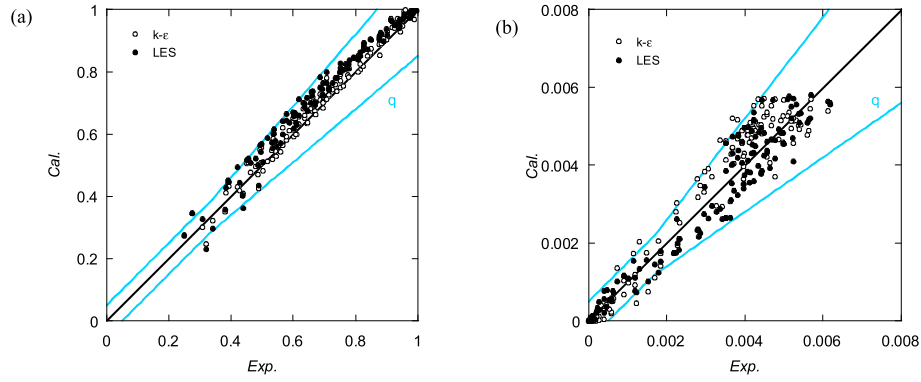
Fig. 15. Scatter plots of numerical simulation results against experimental data for the staggered urban-like cube array: (a) Normalized mean wind speed and (b) Normalized Reynolds stress $-\overline{uw}$. Blue lines mark the threshold for hit rate q. (For interpretation of the references to colour in this figure legend, the reader is referred to the Web version of this article.)

Table 6
Hit rate q for the predicted mean wind speeds and Reynold stresses in the staggered cube array.

Turbulence Model	q	
	U/U_{ref}	$-\overline{uw}/U_{ref}^2$
Modified $k-\varepsilon$	0.989	0.917
LES	0.961	0.982

fine enough for engineering applications.

To model topography in numerical simulations, a two-dimensional interpolation method that combines triangle-based linear and cubic interpolations is recommended to calculate the elevation of topography at grid nodes of the bottom boundary as:

$$h_{node} = \begin{cases} h_{node}^{cubic} & \min(h_{DEM,i}) \le h_{node}^{cubic} \le \max(h_{DEM,i}) \\ h_{node}^{linear} & else \end{cases} , \; i = 1, 2, 3, 4 \quad (19)$$

where the h_{node} is the elevation of topography at grid nodes of the bottom boundary. h_{node}^{linear} and h_{node}^{cubic} are the calculated elevations from DEM by using triangle-based linear and cubic interpolation methods, respectively. $h_{DEM,i}$ are the elevations of closest surrounding four locations from DEM. The σ grid system is recommended to modify the vertical coordinate of grid nodes above the topography. An example of the σ grid system is shown in Fig. 2.

All types of land-use are classified into 11 categories by Ministry of

Land, Infrastructure, Transport and Tourism of Japan (MLIT) and the corresponding roughness lengths z_0 for each category are listed in Table 3 with resolution of $100m \times 100m$. In this study, land use categories for "Buildings" and "Forest" are modelled by the canopy model and others are modelled by the roughness length model. The roughness lengths at the places described by the canopy model is treated as same as that of barren land denoted by the modified roughness length z_0^* and the roughness length at the places without the canopy model is the same as that for the original type of land-use. The information on the shape and height of buildings and vegetation are not included in the land-use database, thus the digital maps are used as shown in section 3.2.

3.2. Digital maps and height identification

In this study, a digital map on buildings called as Zmap-TOWNII and published by ZENRIN is used. As shown in Table 4, it provides the position and shape of buildings by a polygon in vector format and number of floors in integer. Fig. 3 shows the comparison of the distribution of buildings extracted from the digital map with those by the satellite photograph. It is confirmed that the positions and shape of buildings are well reproduced. Though there are some discrepancy due to identification errors or urban redevelopments, the shape file extracted from the digital map can be locally modified based on Google Earth. To determine the average floor height, a photographical measurement is conducted using Street View provided in Google Earth. Some samples of the measured heights at the different locations in Miyakojima island are shown in Fig. 4 and give an average floor height H_{floor} of 3 m, which is calculated by dividing the measured heights of buildings with number of floors.
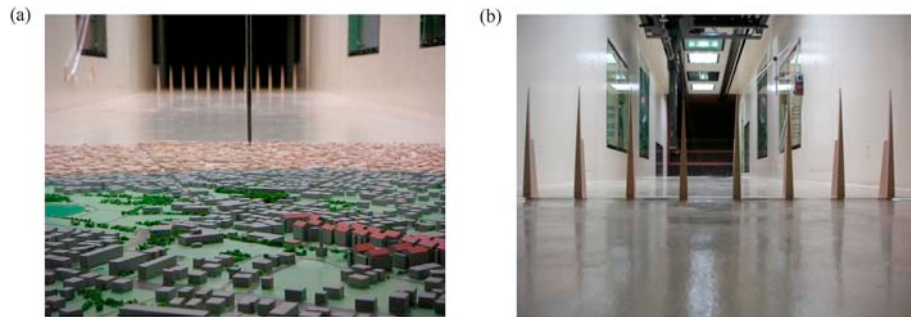

Fig. 16. Overview of the wind tunnel test with (a) a physical urban model and (b) spires in the upstream.
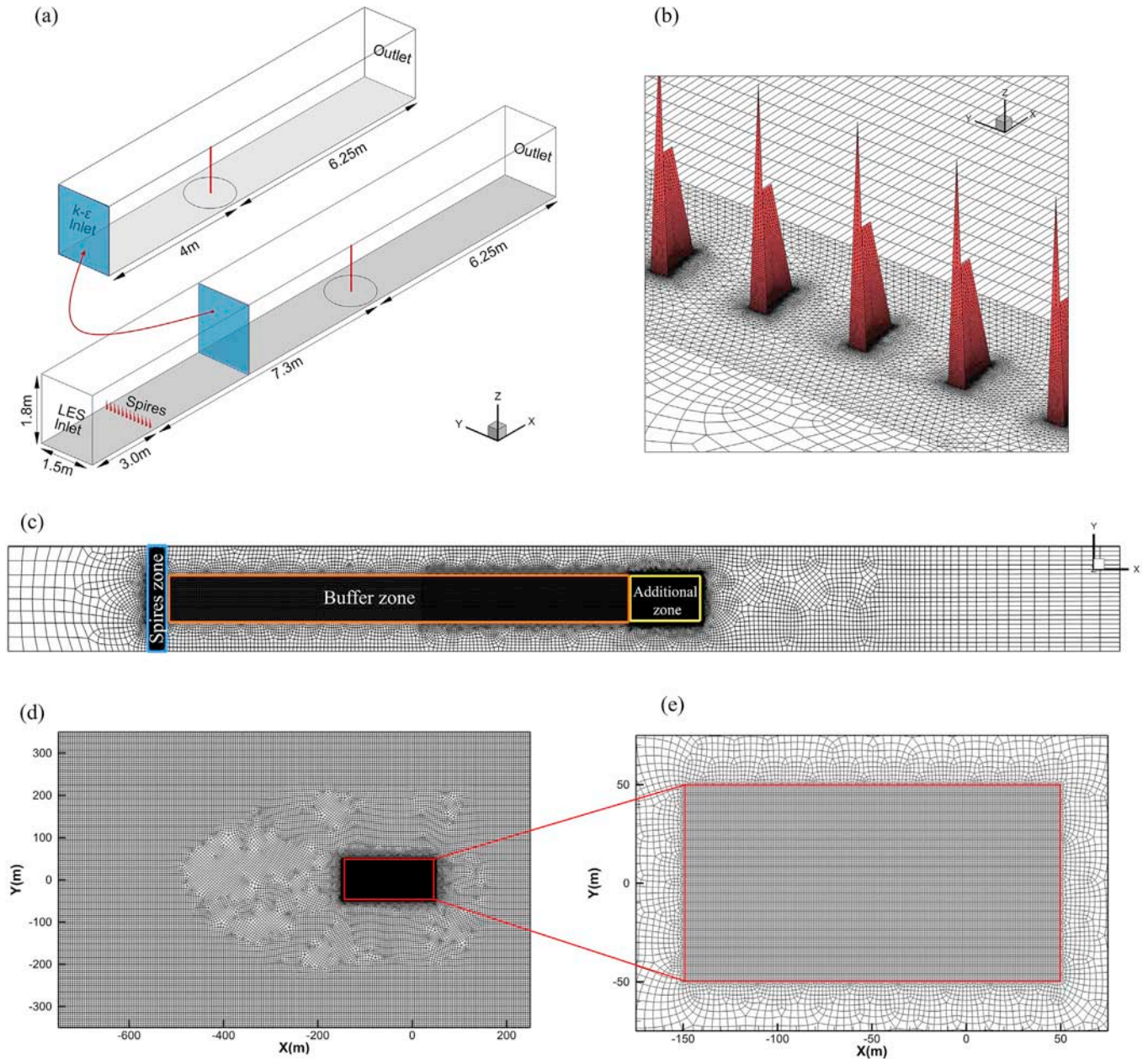
Fig. 17. Configuration of the numerical wind tunnel: (a) bird view of computational domain for LES and modified $k - \varepsilon$ model; (b) grid on spires in numerical simulation; (c) grid system, including the buffer zone and the fine grid zone in the urban area; (d) grid arrangement in the additional and target zones around the station at full scale.

For the vegetation, Natural Environmental Information GIS (hereafter NEI-GIS) provided by Biodiversity Center of Japan is used. Similar as the digital map on buildings, it also provides the position and shape by a polygon in vector format and the type of vegetation in integer (see Table 5). To verify the accuracy of the digital map on vegetation, one example is shown in Fig. 5. It can be clearly seen that, comparing with the satellite photograph, the position and shape of the forest are favorably captured by the digital map from NEI-GIS. Similarly, the vegetation shape file extracted from the digital map can also be locally modified based on Google Earth if there is any discrepancy. In addition, the average height of four representative types of forest are also identified based on Street View in Google Earth as shown in Fig. 6.

3.3. Calculation of canopy parameters from digital maps

In this study, the calculation of canopy parameters for buildings and vegetation from digital maps are different, where b and v are used for variables of buildings and vegetation, respectively.

The three-dimensional shape of buildings with index n ($n = 1, ..., N$) are shown in Fig. 7, where the height of building, h_n^b is the product of height of floor and number of floors from the digital map on buildings. The height of one floor is set as 3 m in this study, and number of floors of 2 is used for the case in which the information of the building is absent in the digital map on buildings.

As shown in Fig. 8, to obtain the packing density γ_0 and representative length l_0 in the computational cell for calculation of fluid force, the
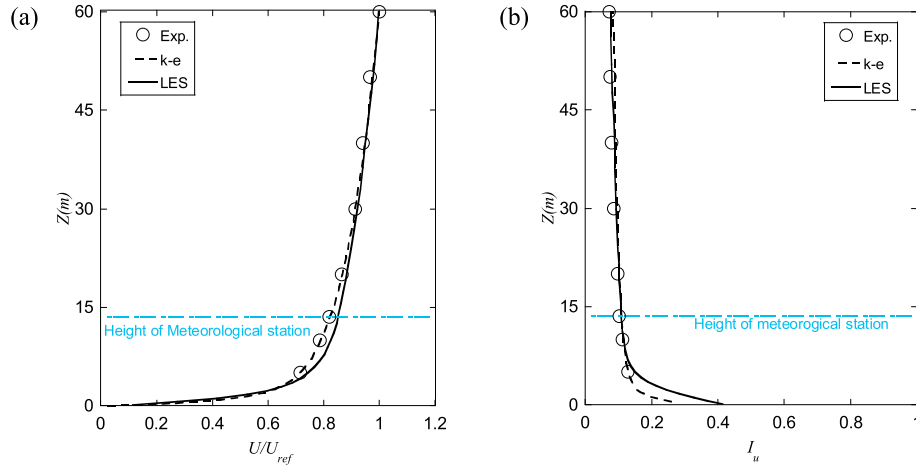
Fig. 18. Vertical profiles of inflow: (a) mean velocity and (b) turbulence intensity. The dashed lines show the height of measurement at the meteorological station.

horizontal occupied area, permieter and effective height in the computational cell are needed to be obtained.

Firstly, the effective height $dh_{n,k}^b$ of building is calculated by Eq. (20).

$$dh_{n,k}^b = \begin{cases} dz_k & (h_n^b > z_k) \\ h_n^b - z_{k-1} & (z_{k-1} < h_n^b < z_k) \end{cases} \qquad (20)$$

$$z_k = \sum_{q=0}^{k} dz_q, \; dz_0 = 0, \; k \geq 1 \qquad (21)$$

where dz_k is the height of the kth cell in the vertical direction, which starts from ground and the height z_k is calculated by Eq. (21). Similarly, the effective height $dh_{t,k}^v$ of vegetation in the computational cell is calculated by Eq. (22).

$$dh_{t,k}^v = \begin{cases} dz_k & (h_t^v > z_k) \\ h_t^v - z_{k-1} & (z_{k-1} < h_t^v < z_k) \end{cases} \qquad (22)$$

Secondly, when the area of buildings or vegetation is overlapped with the boundary of computational cell, the original area is clipped into smaller one by the boundary of computational cell for calculation of horizontal occupied area P_n^b, P_t^v and perimeter C_n^b in this cell. In this study, the method proposed by Sutherland and Hodgman (1974) (hereafter SH method) is applied to clip polygon with the boundary of computational cell.

The SH method is interpreted in Fig. 9, in which the polygon is the target and clipping window marks the boundary of computational cell, and the expected output is the remaining polygon within the clipping window. The SH method firstly identifies whether vertexes of input polygon inside or outside the clipping window, and then builds the output polygon by connecting inside vertexes and points of intersection of input polygon and boundary of clipping window. On identification of position relationship between vertexes of input polygon and boundaries of computational cell, four cases are given in Fig. 10 in the order of scanning each side of polygon anticlockwise. For an arbitrary selected side of input polygon, index s and p represent the start vertex and the end vertex, respectively. In case 1, both vertex s and p are inside the clipping window thus will be used in output polygon. In case 2, the start vertex s and p are inside and outside of the clipping window respectively and the point of intersection is marked with the index c. Then vertexes s and c will be used in output polygon. In case 3, both vertex s and p are outside of the clipping window, thus none of them will be used in the output polygon. Finally, in case 4, the start vertex s and p are outside and inside of the

clipping window, respectively, therefore the vertex p and the point of intersection c will be used in the output polygon. As shown in Fig. 9, the output polygon is built by scanning each side of input polygon and conduct the same operation. The SH method is capable to any polygon on representing shape of single building, group of buildings and vegetation, then occupied area and perimeter of polygon within the computational cell can be calculated.

The packing density γ_0^b of buildings in one computational cell is the ratio of the summation of volume of buildings in this cell and the volume of the cell itself, where the volume of building in a cell is the product of its occupied area P_n^b and height $dh_{n,k}^b$ in this cell. Thus, the packing density of buildings in the computational cell γ_0^b can be calculated by Eq. (23). According to assumption that the fluid force in one computational cell is the summation of fluid force contributed from each building in this computational cell, the representative length l_0^b and he equivalent drag coefficient C_f^b are calculated by Eqs. (24) and (25), respectively, which is following the research done by Maruyama (1993).

$$\gamma_0^b = \gamma_u = \frac{\sum_n P_n^b dh_{n,k}^b}{V_{grid}} \qquad (23)$$

$$l_0^b = \frac{4V_u}{S_u} = \frac{4\sum_n P_n^b dh_{n,k}^b}{\sum_n C_n^b dh_{n,k}^b} \qquad (24)$$

$$C_f^b = \frac{1}{(1-\gamma_0^b)^3} \min\left(\frac{1.53}{(1-\gamma_0^b)}, 2.75(1-\gamma_0^b)\right) \qquad (25)$$

Considering that the scale of leaves is much smaller than the scale of computational cell, the vegetation is treated as a homogeneous medium. The information for a type of vegetation τ, including the height of vegetation h_τ^v, the drag coefficient $C_{f,\tau}^v$, the packing density $\gamma_{0,\tau}^v$ and the representative length $l_{0,\tau}^v$ are provided in the area described by a polygon in vector format. As shown in Figs. 7 and 8, the area occupied by vegetation is represented by a column with index t ($t = 1, \ldots, T$), and height h_t^v. Calculation of packing density $\gamma_{0,t}^v$, representative length $l_{0,t}^v$ and drag coefficient $C_{f,t}^v$ are given in Eqs. (26)–(28), respectively.

$$\gamma_{0,t}^v = \frac{dh_{t,k}^v}{dz_k}\gamma_{0,\tau}^v \qquad (26)$$

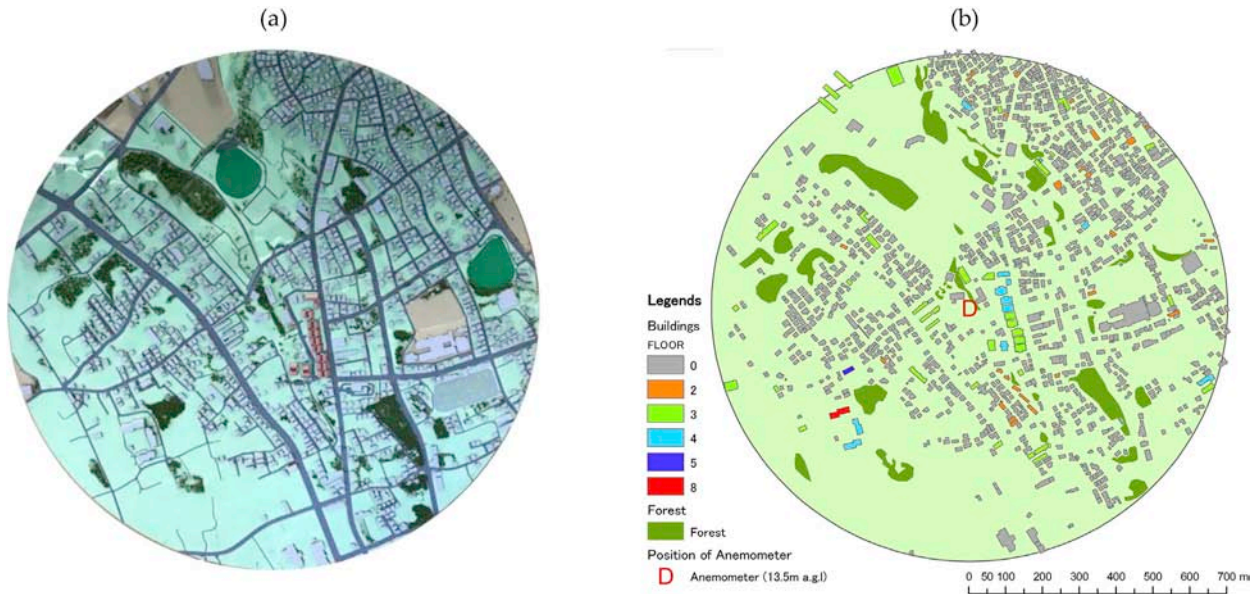$$l_{0,t}^v = l_{0,\tau}^v \qquad (27)$$

(a)

(b)

Fig. 19. Urban model including buildings and vegetation around the meteorological station in Miyakojima island: (a) physical urban model in wind tunnel test and (b) numerical urban model based on the digital maps.

$$C_{f,t}^v = C_{f,\tau}^v \tag{28}$$

3.4. Formulation of fluid force in the mixed land use condition

To consider the mixed land use condition in the real urban area, the fluid force in a computational cell with mixed types of obstacles can be calculated by the sum of those from buildings and vegetation. Firstly, the fluid forces $f_{\overline{u},i}^b$ induced by buildings are calculated based on the canopy parameters of C_f^b, γ_0^b and l_0^b. For vegetation, the sum flux in one computational cell $f_{\overline{u},i}^v$ is calculated by averaged flux weighted with the area of different types of vegetation in the computational cell, which follows the approach by Kimura (1989) as shown in Eq. (29).

$$f_{\overline{u},i} = f_{\overline{u},i}^b + f_{\overline{u},i}^v = C_f^b \frac{\gamma_0^b}{l_0^b} \frac{\rho}{2} |\overline{u}|\overline{u}_i + \sum_t \left(\eta_t^v C_{f,t}^v \frac{\gamma_{0,t}^v}{l_{0,t}^v} \right) \frac{\rho}{2} |\overline{u}|\overline{u}_i \tag{29}$$

where, η_t^v is the occupied area ratio defined by the horizontal area of one type of vegetation P_t^v over the horizontal area of one computational cell S_{grid} as shown in Eq. (30).

$$\eta_t^v = \frac{P_t^v}{S_{grid}} \tag{30}$$

However, it is inefficient to maintain parameters for each building and vegetation in the engineering application. Therefore, the canopy parameters in the mixed land-use area are described as the equivalent drag coefficient C_f, pecking density γ_0, and representative length l_0 as shown in Eq. (1). The packing density is defined as the ratio of summation of volume of all obstacles inside the computational cell over the volume of the computational cell as:

$$\gamma_0 = \gamma_0^b + \sum_t \left(\eta_t^v \gamma_{0,t}^v \right) \tag{31}$$

The representative length l_0 is determined as the maximum one in the computational cell, which dominants the representative turbulence scale generated by obstacles:

$$l_0 = \max \left(l_0^b, l_{0,t}^v \right) \quad (t = 1, \dots, T) \tag{32}$$

Then equivalent drag coefficient C_f can be derived based on the relationship between Eqs. (1), (29), (31) and (32), as shown in the following equation:

$$C_f = \frac{l_0}{\gamma_0} \left[C_f^b \frac{\gamma_0^b}{l_0^b} + \sum_t \left(\eta_t^v C_{f,t}^v \frac{\gamma_{0,t}^v}{l_{0,t}^v} \right) \right] \tag{33}$$

Through the transformation from the digital maps into the canopy parameters of the generalized canopy model, it is capable to predict the flow field over the urban area from a single building or tree to a whole city without changing models and boundary conditions. As a summary, the buildings and vegetation in this study are simulated by the canopy model, while other surface roughness are calculated by the roughness length model with roughness length z_0 from land-use database as shown in Table 3.

4. Numerical results of urban-like cube arrays

Numerical setups of the urban-like cube arrays, including the computational domain and grid system for each case, are described in section 4.1. The numerical results of turbulent flow fields in the urban-like cube arrays are discussed in section 4.2. The predicted turbulent flow fields are compared with the experimental results and the accuracy is evaluated by the validation metrics for the modified $k - \varepsilon$ and LES turbulence models.

4.1. Numerical setups of the urban-like cube arrays

The wind tunnel test carried out by Maruyama (1993) is selected for validation of the predicted turbulent flow fields over the staggered cube arrays. This experiment was carried out in an open circuit wind tunnel with a test section of 2.5 m wide, 2.0 m high and 21 m long. A uniform inflow was set at about 10 m/s, and about 13 m in the longitudinal direction was covered by the staggered cube arrays with the height of 0.03 m. Three different packing densities, 5.6%, 12.5% and 25%, of staggered cube arrays were studied experimentally. The layouts of the staggered
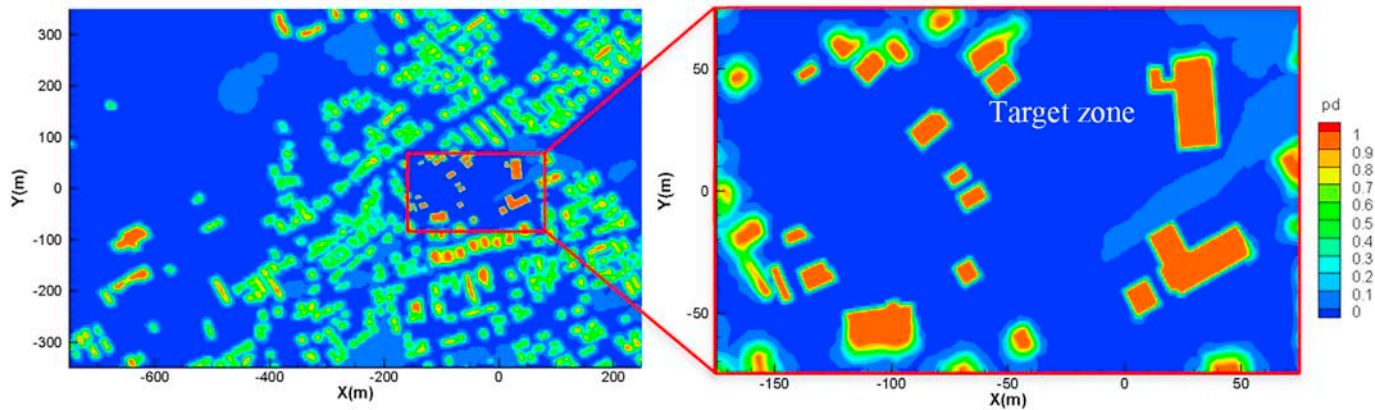
Fig. 20. Distribution of packing density in the additional and target zones obtained from the digital maps at full scale.
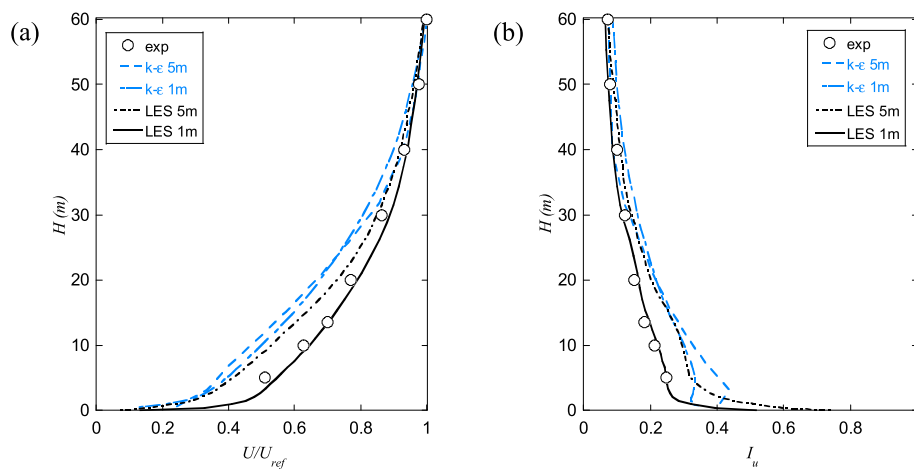

Fig. 21. Wind profiles of (a) mean wind speed and (b) turbulence intensity in south direction predicted by the modified $k - \varepsilon$ and LES turbulence models with different grid resolutions.

cube arrays with different packing density are illustrated in Fig. 11.

The configuration of the computational domain used for LES simulation generally follows the wind tunnel test setup and presented in Fig. 12, where the roughness canopy starts from $x = 0$ m, and ends at $x = 13.1$ m. The profiles of mean wind speed U and Reynold stress $-\overline{u'w'}$ were measured at four positions of $x = -0.9$ m (P0), $x = 1.3$ m (P1), $x = 3.7$ m (P3), $x = 6.2$ m (P4) in the longitudinal direction. Although no boundary layer generator was set in the wind tunnel test, turbulent boundary layer with the height of about 0.17 m generated by the floor of wind tunnel, was observed at position P_0. The height of turbulent boundary layer is higher than the height of cubes and may affect the turbulent flow field in the canopy. Thus, in the LES simulations, two rows of blocks of 0.045 m high followed by another block canopy of 0.014 m high are introduced as a boundary layer generator in the upstream part of the numerical wind tunnel as shown in Fig. 12. Considering the homogeneously distributed cubes, the length and width of the numerical wind tunnel are set as 19 m and 1 m, respectively. And, the height is kept the same as that of the wind tunnel. For simulation with the modified $k- \varepsilon$ model, a shorter domain with length of 17 m is used, while the height and width are kept the same as those in LES simulation.

For simulations with LES turbulence model, uniform horizontal (x-y plane) grid resolution of 0.03 m, is applied in the region of staggered cube array. At the bottom and the top of the canopy region the vertical grid size is 0.0005 m. The maximum vertical grid size in canopy is 0.003

m and the number of grid along the height of canopy is 10. Above the top of the canopy, the grid starts from 0.0005 m and grows with a ratio of 1.1. For simulations with modified $k - \varepsilon$ model, uniform horizontal grid resolution of 0.06 m is used and the vertical grid resolution is kept the same as that in LES model.

In simulations with the modified $k - \varepsilon$ model, the logarithmic law is used on the ground surface with the roughness height of $z_0 = 7 \times 10^{-5} m$. The turbulent inflow profiles of $U(z)$, $k(z)$ and $\varepsilon(z)$ are directly imposed at the inlet boundary. While in simulations with LES turbulence model, a uniform wind speed $U(z) = 10$ m/s is set at the inlet boundary. The distribution of cube arrays is imported in the format of digital map, and canopy parameters of C_f, γ_0 and l_0, are then calculated by the approach described in section 3.

4.2. Mean wind speed and Reynolds stress in the urban-like cube arrays

The predicted mean wind speed and Reynolds stress at the position P_0 are shown in Fig. 13. It can be seen that an accurate inflow at the position in front of the edge of staggered cube arrays is achieved in the simulations with the modified $k - \varepsilon$ and LES turbulence models. The predicted mean wind speed and Reynolds stress at the measurement positions by the modified $k - \varepsilon$ and LES turbulence models are averaged in the lateral direction and shown in Fig. 14. The mean wind speed U_{ref} at z/H = 15 at the position P_0 is used for normalization. The bold solid line marks the
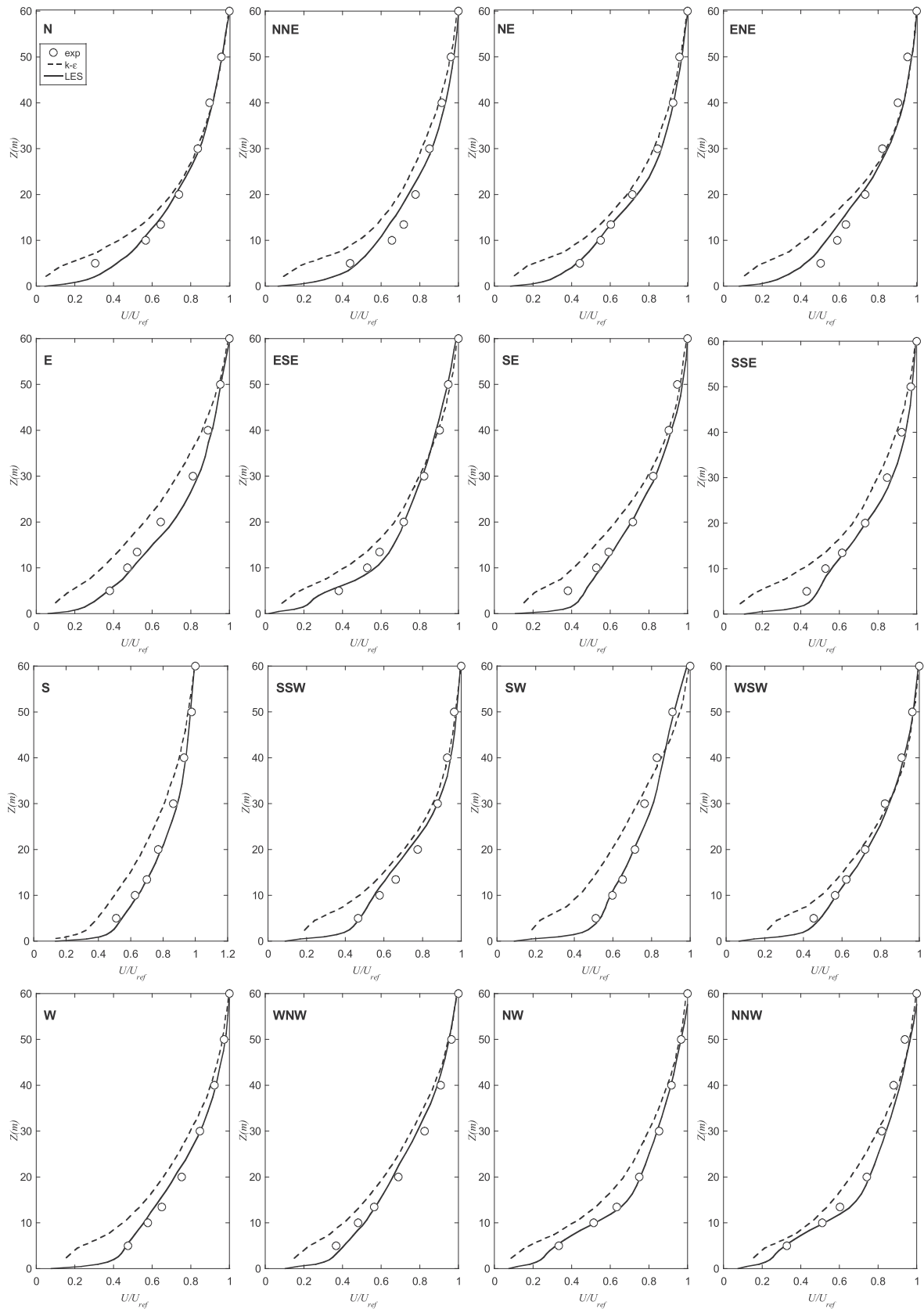
Fig. 22. Vertical profiles of mean wind speed at the target site in each wind direction. Open circles denote experimental data, dash lines are results predicted by the modified $k - \varepsilon$ model, and solid lines represent values obtained from LES simulation.
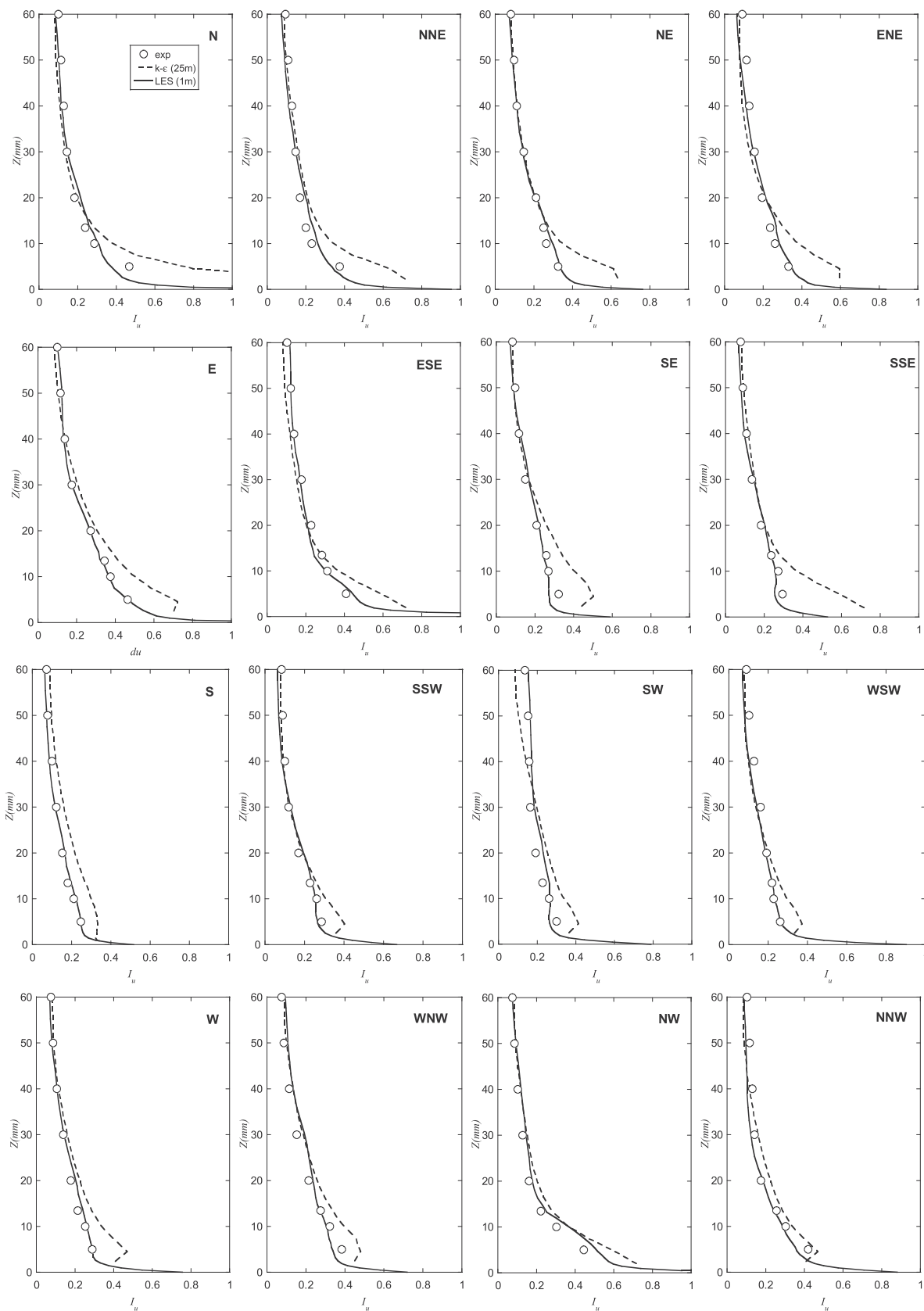
Fig. 23. Vertical profiles of turbulence intensity at the target site in each wind direction. Open circles denote experimental data, dash lines are results predicted by the modified $k - \varepsilon$ model, and solid lines represent values obtained from LES simulation.
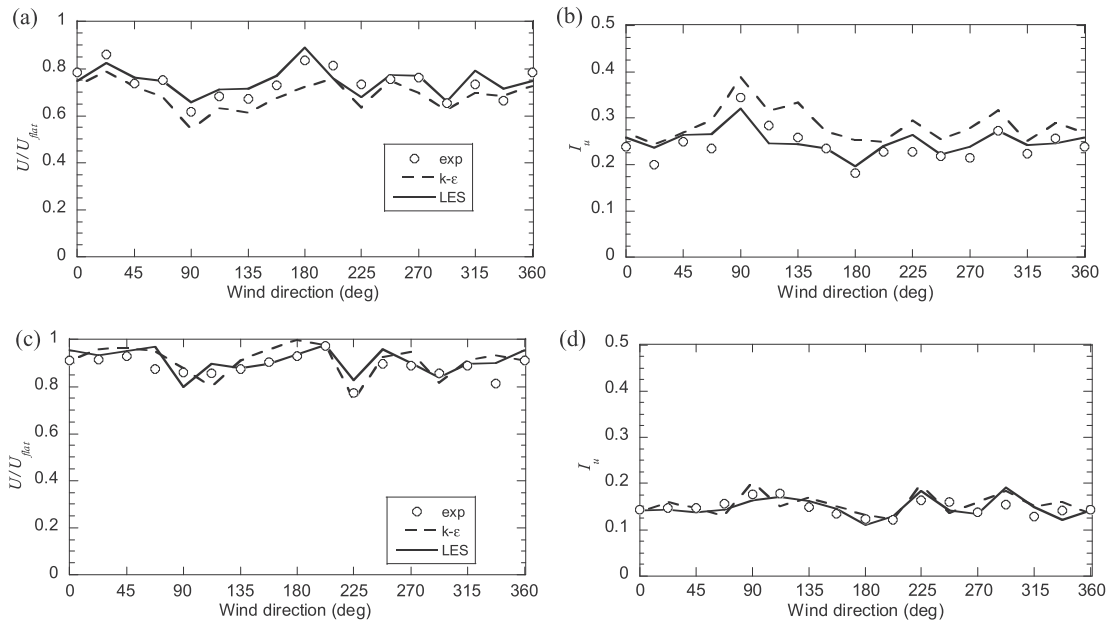
Fig. 24. Comparison between simulation results and experimental data against different wind directions: (a) wind speed ratio and (b) turbulence intensity the height of 13.5 m, (c) wind speed ratio and (d) turbulence intensity the height of 30 m.
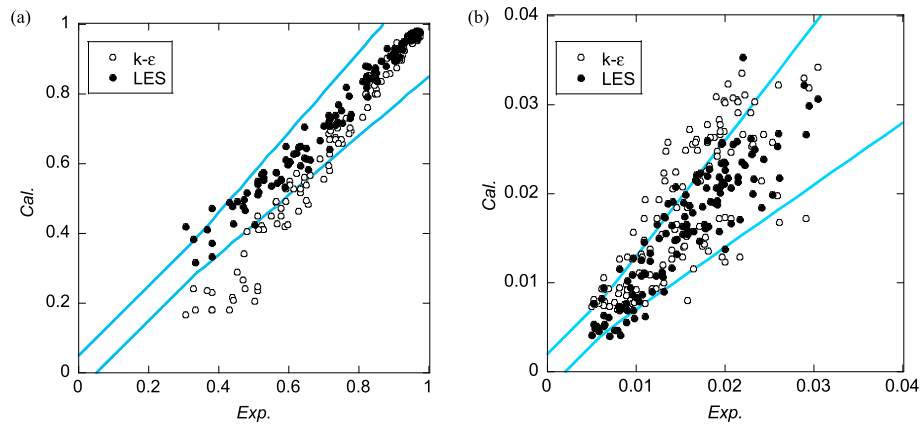

Fig. 25. Scatter plots of numerical simulation results against experimental data for the real urban area: (a) normalized mean wind speed U/U_{ref}, (b) normalized Reynolds stress $\overline{uu}/U_{ref}^2$. Blue lines mark the threshold for hit rate q. (For interpretation of the references to colour in this figure legend, the reader is referred to the Web version of this article.)

boundary of canopy occupied by the staggered cube arrays and dash dot lines indicate the measurement positions. It is found that both modified $k - \varepsilon$ and LES turbulence models show good agreement with the experimental data for all cases with different packing densities. The development of height of boundary layer is also well captured in the longitudinal direction. The vertical profiles of Reynolds stress $-\overline{uw}$ over the staggered cube arrays are normalized by U_{ref}^2 as shown in Fig. 14. Good agreements are also achieved by both modified $k - \varepsilon$ and LES turbulence models for all packing densities. The maximum Reynolds stress generated by the staggered cube arrays is observed at the top of canopy, and the turbulence decreases as the height increases.

To quantitatively evaluate the performance of the modified $k - \varepsilon$ and LES turbulence models, the validation metrics q is used. Scatter plots of numerical results against experimental data are shown in Fig. 15, in which the blue lines mark the boundaries defined by validation metrics q. Validation metrics are also summarized in Table 6. The hit rates for the

mean wind speed and Reynold stress by both turbulence models are close to one, which indicates both the modified $k - \varepsilon$ and LES models in cooperate with the generalized canopy model are able to provide accurate prediction on turbulent flow above the uniform urban canopy with different packing density.

5. Numerical results of real urban areas

Numerical setups of real urban areas for the modified $k - \varepsilon$ and LES turbulence models, including the computational domain and grid system, are described in section 5.1. The numerical results of turbulent flow fields in real urban areas are discussed in section 5.2. The predicted turbulent flow fields are compared with the experimental results and the accuracy is evaluated by the validation metrics for the modified $k - \varepsilon$ and LES turbulence models.

Table 7
Hit rate q for the predicted mean wind speed and turbulence intensity in the real urban area.

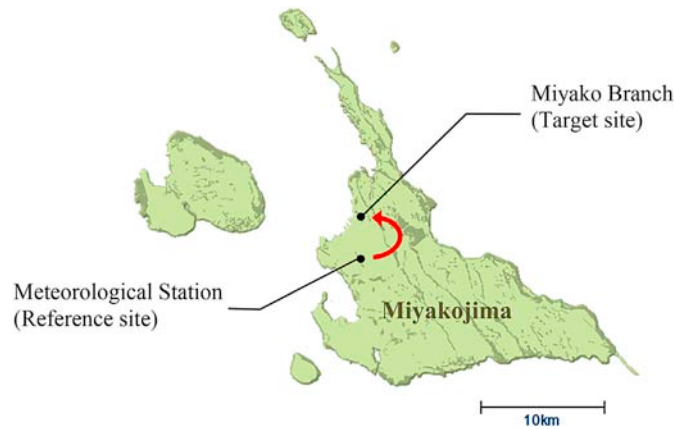| Turbulence Model	q	
	U/U_{ref}	$\overline{uu}/U_{ref}^2$
Modified $k-\varepsilon$	0.643	0.571
LES	0.964	0.848

Fig. 26. Overview of the Miyakojima island with the locations of meteorological station and Miyako Branch of Okinawa Electricity Power Company.

5.1. Numerical setups of real urban areas

Typhoon Maemi struck the Miyakojima island of Japan in 2003 and more than 1000 utility poles and 7 wind turbines were extensively damaged (Ishihara et al., 2005b). In order to improve the safety of these structures, it is necessary to accurately estimate the maximum wind speed at the locations of structures. Although time series of wind speeds and directions were recorded at the Miyakojima meteorological station, they cannot be directly used to estimate the maximum wind load because the station is located in the urban area and the observed wind speed is strongly affected by the surrounding buildings. A wind tunnel test as shown in Fig. 16 was carried out by Ishihara et al. (2005a) to estimate the mean wind speeds and turbulence intensities in the urban area of Miyakojima island, in which the spires were used to provide the inflow of atmospheric boundary layer. However, it is expensive and time consuming to conduct a wind tunnel test, especially to measure the mean wind speeds and turbulence intensities at the locations of poles in 16 wind directions. In this study, a numerical wind tunnel considering the effects of buildings and trees is built to predict the turbulent flow field at the meteorological station and compare with those obtained by the wind tunnel test.

The configuration of the numerical wind tunnel used for LES and modified $k-\varepsilon$ model is presented in Fig. 17. In LES simulation, the spires (see Fig. 17(b)) are built upstream the urban model to generate the neutrally stratified atmospheric boundary layer following the wind tunnel test, where the computational domain is 1.5 m wide, 1.8 m high and 17.7 m long as same as the test section of wind tunnel (Fig. 17(a)). For the numerical simulations by the modified $k-\varepsilon$ model, a shorter domain excluding spires with length of 11.3 m is used, where the values of mean velocity $U(z)$ and Reynolds stress $\overline{u_iu_j}(z)$ extracted at the location of $x = -4$ m from the LES simulations are imposed at the inlet boundary. Assuming local equilibrium of production and dissipation of turbulence kinetic energy $\frac{1}{2}P_{ii} = \rho\varepsilon$ in streamwise direction (Mochida et al., 2002),
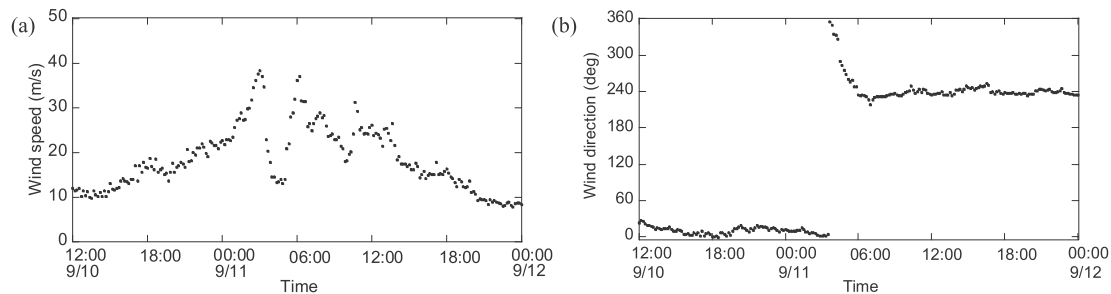

Fig. 27. Observed 10-min-average wind speed and direction at the meteorological station: (a) wind speed and (b) wind direction.
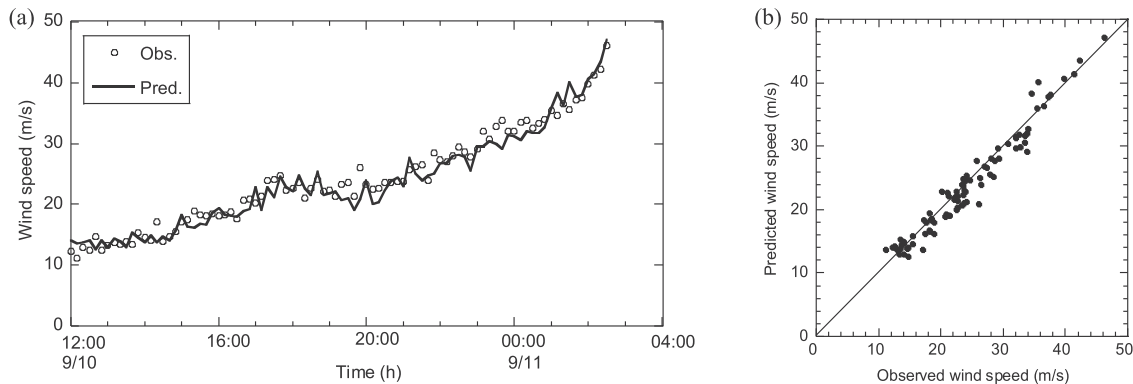

Fig. 28. Comparison of predicted and observed wind speeds at the Miyako Branch: (a) 10-min-average wind speeds and (b) scatter plots.

$k(z)$ and $\varepsilon(z)$ at the inlet are given by:

$$k(z) = \frac{1}{2}\overline{u_i u_i}(z) \tag{34}$$

$$\varepsilon(z) = -\overline{u_1 u_3}\frac{dU(z)}{dz} \tag{35}$$

The location of meteorological station is set as the origin of the computational domain. For the sake of reducing calculation cost as well as keeping prediction accuracy, a hybrid grid system is designed as shown in Fig. 17 (c). A target zone to consider the surrounding buildings is a rectangular area of 100 m wide and 200 m long as shown in Fig. 17 (d), where the grid resolution of 1 m is applied based on a grid dependency test discussed below. An additional zone starts from 800 m upstream to 250 m downstream with a width of 700 m and is appended to the target zone, where the grid is generated with a resolution of 5 m. The unstructural grid with a relative coarse resolution is used in the buffer zones. It is noted that the grid system generated in current study is in line with practice guidelines (Casey and Wintergerste, 2000; Tucker and Mosquera, 2001; Iousef et al., 2017). The maximum grid growth ratio between adjacent subdomains is set to 1.15 in this study, which is following the hybrid grid setting used in the numerical simulation on complex terrain covered by canopy layers (Liu et al., 2016; Qian and Ishihara, 2019).

Firstly, the LES simulation with spires is performed to generate the atmosphere boundary layer over the flat terrain. The vertical profiles at the target site are presented in Fig. 18, where the measured data obtained from the wind tunnel test are also plotted for comparison. The mean wind speed U is normalized by the reference value U_{ref} at the height of 60 m at full scale, and the turbulence intensity is defined as the ratios of standard deviation of fluctuating wind speed σ_u to mean wind speed U at each height. The incident profiles of turbulence used in the modified $k - \varepsilon$ model by using the approach described in section 5.1 are also plotted for comparison. It is observed that the predicted mean wind speed and turbulence intensity show good agreement with the experimental data, which implies that the inflow condition is well reproduced as that in the wind tunnel test.

Subsequently, as shown in Fig. 19 (b), the numerical urban model with a scale of 1:1000 and a radius R = 700 m is generated. The buildings and trees are reproduced by the method presented in section 3.2, where the shape and height are modified to exactly match with those in the wind tunnel test as shown in Fig. 19 (a). The local topography is also considered based on the digital elevation model with a resolution of 10 m. The urban canopies in the areas with the distance from the meteorological station of 700–1320 m are also included at the upwind side as set in the wind tunnel test.

The numerical urban model is then imported and clipped by the hybrid grid system. Fig. 20 shows the contour of packing density extracted from the first layer of cells in the computational domain for the southerly wind. In the target zone, it is observed that the shape of buildings is quite distinct since the high resolution grid is applied, while the outlines of buildings are not clearly captured in the additional zone.

5.2. Mean wind speed and turbulence intensity in real urban areas

A grid dependency test is conducted at the meteorological station, where two grid resolutions of 5 m and 1 m are tested by using the modified $k - \varepsilon$ and LES turbulence models, respectively. The vertical profiles of predicted mean velocity and turbulence intensity for the southerly wind are compared with the experimental data in Fig. 21, where the reference value U_{ref} at the height of 60 m is used for normalization.

The modified $k - \varepsilon$ model generally provides grid independent results with two different grid resolutions. The turbulent flow filed at the

high elevation over 30 m are well predicted, while the mean wind speed at the low elevation is underestimated and the turbulence intensity is overestimated. In regions close to the ground in urban area, the organized motions due to the vortex shedding in wake of buildings dominate the turbulent flow filed. As investigated by Qi and Ishihara (2018), Ishihara and Qi (2019), those organized motions cannot be captured by the modified k-ε model, therefore the predicted profiles show discrepancies with experimental data. However, in the high elevation region above the buildings, the turbulent flow field is fully developed and thus can be well reproduced by the modified k-ε model. The LES simulation with the grid resolution of 5 m also underestimates the mean wind speed and overestimates the turbulence intensity at the low elevation, while the grid resolution of 1 m provides favorable agreement with the wind tunnel test for both mean wind speed and turbulence intensity.

The numerical simulations are performed in the 16 wind directions by using the modified $k - \varepsilon$ and LES turbulent models with the finest grid resolution of 1 m for further validation. The vertical profiles of mean wind speed and turbulence intensity at the meteorological station in 16 wind directions are summarized in Figs. 22 and 23, where the measured data from the wind tunnel test are also plotted for comparison. It is found that the modified $k - \varepsilon$ model generally gives large error at the low elevation, while the LES turbulence model shows good agreement with the experimental data at both low and high elevations. The predicted mean wind speed and turbulence intensity at the height of 13.5 m and 30 m are extracted and compared with the experimental data in 16 wind directions as shown in Fig. 24, where the mean wind speed are normalized by U_{flat} at the corresponding height simulated over the flat terrain. It is noticed that, at the height of 13.5 m, both mean wind speed and turbulence intensity predicted by the LES turbulence model well fit the experimental data, while at the high elevation of 30 m, the modified $k - \varepsilon$ model performs well as the LES turbulence model.

In order to quantitatively evaluate the performance of modified $k - \varepsilon$ and LES turbulence models, validation metrics of hit rate q is applied. Scatter plots of numerical results against experimental data are shown in Fig. 25, in which the mean wind speed at the height of 60 m over flat terrain is used as the U_{ref} for normalization. Validation metrics are summarized in Table 7. The LES turbulence model shows much better performance for both mean wind speed and turbulence intensity in the urban canopy with a higher hit rate than that by the modified $k - \varepsilon$ model.

In order to demonstrate the performance of the developed numerical model to predict wind fields in urban areas, numerical simulations are performed for the Miyakojima island and compared with the observed wind speed during Typhoon Maemi. The wind speed ratio C_{pr}, and the changes in the wind direction $\Delta\theta_{pr}$, between the reference site and the target sites are calculated as a function of wind direction. The wind speed and wind direction at the target site, U_p and θ_p, are estimated by multiplying the wind speed ratio and adding the change in the wind direction to the observed wind speed, U_r, and wind direction, θ_r, at the reference site and expressed as Eqs. (34) and (35) as shown by Misu and Ishihara (2018):

$$U_p(t) = U_r(t) \times C_{pr} \tag{36}$$

$$\theta_p(t) = \theta_r(t) + \Delta\theta_{pr} \tag{37}$$

where subscripts p, r, and pr denote the target site, the reference site, and the relationship between target and reference sites, respectively. The wind speed ratio, and the change in the wind direction is obtained by the liner interpolation based on the values from the numerical simulations in 16 wind directions.

As shown in Fig. 26, the meteorological station and Miyako Branch of Okinawa Electricity Power Company are set as the reference and target sites, respectively in this study. The 10-min-average wind speed and wind direction recorded at the meteorological station during Typhoon Maemi

are shown in Fig. 27 (Ishihara et al., 2005a). Sudden changes in wind speed and wind direction were observed when the center of the typhoon passed right over the island at 3 a.m. on September 11, 2003. The wind speeds at the height of 22 m at the Miyako Branch are predicted and compared with the observed data as shown in Fig. 28. It can be clearly seen that the predicted wind speeds show good agreement with the observation and the coefficient of determination is 0.96. The observed data was not obtained at the Miyako Branch after 2:30 a.m. due to the damage of anemometer.

6. Conclusions

In this study, a digital urban model is proposed. The turbulent flow fields over urban-like cube arrays with different packing densities and a real urban area are investigated by both modified $k - \varepsilon$ and LES turbulence models. The following conclusions are obtained.

(1) A digital urban model is proposed, which includes digital elevation model for topography, the land-use database, digital maps on buildings and vegetation. The canopy model is recommended to apply for buildings and vegetation with the height larger than 2 m, while the roughness length model is used for the lower vegetation as well as other types of roughness. The proposed digital urban model is used to model the real urban areas.

(2) The modified $k - \varepsilon$ model is less sensitive to the grid resolution and is able to predict turbulent flow fields over uniform urban-like cube arrays with different packing densities, where the turbulent flow fields are fully developed. The modified $k - \varepsilon$ model fails to predict turbulent flow fields in non-uniform urban areas, where the turbulent flow fields is strongly affected by the organized motions generated by surrounding buildings. In the modified k-ε model, only the source term to consider the effects of canopy are added to the governing equations, thus no additional equation needs to be resolved and no extra cost is added compared with the standard one.

(3) The LES turbulence model is able to predict turbulent flow fields over uniform urban-like cube arrays as well as in non-uniform urban areas and shows good agreement with the wind tunnel test and field measurement. The LES turbulence model is strongly affected by the grid resolution and the grid convergence test is necessary for the local target zone.

CRediT authorship contribution statement

Takeshi Ishihara: Resources, Conceptualization, Methodology, Supervision, Writing - review & editing. **Guo-Wei Qian:** Investigation, Software, Writing - original draft, Formal analysis, Visualization. **Yi-Hong Qi:** Data curation, Validation.

Declaration of competing interest

The authors declare that they have no known competing financial interests or personal relationships that could have appeared to influence the work reported in this paper.

Acknowledgement

References

Advanced Land Observing Satellite, https://www.eorc.jaxa.jp/ALOS/en/.

Antoniou, N., Montazeri, H., Wigo, H., Neophytou, M.K.A., Blocken, B., Sandberg, M., 2017. CFD and wind-tunnel analysis of outdoor ventilation in a real compact heterogeneous urban area: evaluation using "air delay". Build. Environ. 126, 355–372.

Ashie, Y., Tokairin, T., Kono, T., 2007. High resolution numerical simulation on the urban heat island in a ten-kilometer square area of central Tokyo by using the earth simulator. J. Environ. Eng. 616, 67–74.

Aumond, P., Masson, V., Lac, C., Gauvreau, B., Dupont, S., Berengier, M., 2013. Including the drag effects of canopies: real case large-eddy simulation studies. Boundary-Layer Meteorol. 146 (1), 65–80.

Bailey, B.N., Stoll, R., 2013. Turbulence in sparse, organized vegetative canopies: a large-eddy simulation study. Boundary-Layer Meteorol. 147 (3), 369–400.

Bechmann, A., Sørensen, N.N., 2010. Hybrid RANS/LES method for wind flow over complex terrain. Wind Energy 13 (1), 36–50.

Biodiversity Center of Japan, http://www.biodic.go.jp/trialSystem/top_en.html.

Blocken, B., Stathopoulos, T., Carmeliet, J., 2007. CFD simulation of the atmospheric boundary layer: wall function problems. Atmos. Environ. 41 (2), 238–252.

Blocken, B., Janssen, W., van Hooff, T., 2012. CFD simulation for pedestrian wind comfort and wind safety in urban areas: general decision framework and case study for the Eindhoven University campus. Environ. Model. Software 30, 15–34.

Casey, M., Wintergerste, T., 2000. Best Practices Guidelines: ERCOFTAC Special Interest Group on Quality and Trust in Industrial CFD. Ercoftac.

Cheng, W.-C., Porté-Agel, F., 2015. Adjustment of turbulent boundary-layer flow to idealized urban surfaces: a large-eddy simulation study. Boundary-Layer Meteorol. 155 (2), 249–270.

Coceal, O., Thomas, T.G., Castro, I.P., Belcher, S.E., 2006. Mean flow and turbulence statistics over groups of urban-like cubical obstacles. Boundary-Layer Meteorol. 121 (3), 491–519.

Enoki, K., Ishihara, T.A., Yamaguchi, A., 2009. A generalized canopy model for the wind prediction in the forest and the urban area. Proc. EWEC 2009.

Fluent 16.2, 2015. Theory Guide. Ansys Inc., Canonsburg, PA.

Geospatial Information Authority of Japan, https://www.gsi.go.jp/ENGLISH/index.html.

Giometto, M.G., Christen, A., Egli, P.E., Schmid, M.F., Tooke, R.T., Coops, N.C., Parlange, M.B., 2017. Effects of trees on mean wind, turbulence and momentum exchange within and above a real urban environment. Adv. Water Resour. 106, 154–168.

Google Earth, https://www.google.co.jp/intl/ja/earth/.

Gousseau, P., Blocken, B., Stathopoulos, T., Van Heijst, G.J.F., 2011. CFD simulation of near-field pollutant dispersion on a high-resolution grid: a case study by LES and RANS for a building group in downtown Montreal. Atmos. Environ. 45 (2), 428–438.

Green, S.R., 1992. Modeling turbulent air flow in a stand of widely spaced trees. Phoenics J. Comput. Fluid Dyn. its Appl. 5, 294–312.

Grimmond, C., Oke, T.R., 1999. Aerodynamic properties of urban areas derived from analysis of surface form. J. Appl. Meteorol. 38 (9), 1262–1292.

Gutiérrez, E., Martilli, A., Santiago, J.L., González, J.E., 2015. A mechanical drag coefficient formulation and urban canopy parameter assimilation technique for complex urban environments. Boundary-Layer Meteorol. 157 (2), 333–341.

He, Y., Tablada, A., Wong, N.H., 2018. Effects of non-uniform and orthogonal breezeway networks on pedestrian ventilation in Singapore's high-density urban environments. Urban Clim. 24, 460–484.

Iousef, S., Montazeri, H., Blocken, B., Van Wesemael, P.J.V., 2017. On the use of non-conformal grids for economic LES of wind flow and convective heat transfer for a wall-mounted cube. Build. Environ. 119, 44–61.

Ishihara, T., Qi, Y., 2019. Numerical study of turbulent flow fields over steep terrains by using a modified delayed detached eddy simulations. Boundary-Layer Meteorol. 170, 45–68.

Ishihara, T., Yamaguchi, A., Takahara, K., Mekaru, T., Shinjo, F., 2005a. Evaluation of maximum wind speed during typhoon 0314 using wind tunnel tests and numerical simulation. J. Struct. Eng. A 51, 911–920 (In Japanese).

Ishihara, T., Yamaguchi, A., Takahara, K., Mekaru, T., Matsuura, S., 2005b. An analysis of damaged wind turbines by Typhoon Maemi in 2003. In: Proceeding of the Sixth Asia-Pacific Conference on Wind Engineering, Seoul, Korea, pp. 1413–1428.

Ito, Y., Ishihara, T., 2018. Study on the numerical prediction of strong winds in urban areas. Part 2: Modelling and verification of buildings and trees. In: Proceedings of the 73rd Annual Conference of Japan Society of Civil Engineers, vols. I-291, pp. 581–582 (in Japanese).

Kader, B., 1981. Temperature and concentration profiles in fully turbulent boundary layers. Int. J. Heat Mass Tran. 24 (9), 1541–1544.

Kanda, M., 2006. Large-eddy simulations on the effects of surface geometry of building arrays on turbulent organized structures. Boundary-Layer Meteorol. 118 (1), 151–168.

Kanda, M., Inagaki, A., Miyamoto, T., Gryschka, M., Raasch, S., 2013. A new aerodynamic parametrization for real urban surfaces. Boundary-Layer Meteorol. 148 (2), 357–377.

Kato, M., 1993. The modeling of turbulent flow around stationary and vibrating square cylinders. In: Ninth Symposium on Turbulent Shear Flows.

Kawaguchi, M., 2000. The statistics on the occurrence of strong wind and related damages. In: Wind Disaster Forum. Kyoto.

Kimura, F., 1989. Heat flux on mixtures of different land-use surface: test of a new parameterization scheme. J. Meteorol. Soc. Jpn Ser. II 67 (3), 401–409.

Lien, F., Yee, E., Cheng, Y., 2004. Simulation of mean flow and turbulence over a 2D building array using high-resolution CFD and a distributed drag force approach. J. Wind Eng. Ind. Aerod. 92 (2), 117–158.

Liu, J., Chen, J.M., Black, T., Novak, M.D., 1996. E-ε modeling of turbulent air flow downwind of a model forest edge. Boundary-Layer Methodol. 77, 21–44.

Liu, Z., Ishihara, T., He, X., Niu, H., 2016. LES study on the turbulent flow fields over complex terrain covered by vegetation canopy. J. Wind Eng. Ind. Aerod. 155, 60–73.

Longo, R., Ferrarotti, M., Sánchez, C.G., Derudi, M., Parente, A., 2017. Advanced turbulence models and boundary conditions for flows around different configurations of ground-mounted buildings. J. Wind Eng. Ind. Aerod. 167, 160–182.

Maruyama, T., 1993. Optimization of roughness parameters for staggered arrayed cubic blocks using experimental data. J. Wind Eng. Ind. Aerod. 46, 165–171.

Ministry of Land, Infrastructure, Transport and Tourism (MLIT) of Japan, https://www.mlit.go.jp/en/index.html.

Misu, Y., Ishihara, T., 2018. Prediction of frequency distribution of strong crosswind in a control section for train operations by using onsite measurement and numerical simulation. J. Wind Eng. Ind. Aerod. 174, 69–79.

Mochida, A., Tominaga, Y., Murakami, S., Yoshie, R., Ishihara, T., Ooka, R., 2002. Comparison of various k-e models and DSM applied to flow around a high rise building-report on AIJ cooperative project for CFD prediction of wind environment. Wind Struct. 5 (2–4), 227–244.

Mochida, A., Yoshino, H., Iwata, T., Tabata, Y., 2006. Optimization of tree canopy model for CFD prediction of wind environment at pedestrian level. In: The Fourth International Symposium on Computational Wind Engineering, Yokohama, Japan.

Mueller, E., Mell, W., Simeoni, A., 2014. Large eddy simulation of forest canopy flow for wildland fire modeling. Can. J. For. Res. 44 (12), 1534–1544.

Nozu, T., Tamura, T., Okuda, Y., Sanada, S., 2008. LES of the flow and building wall pressures in the center of Tokyo. J. Wind Eng. Ind. Aerod. 96 (10–11), 1762–1773.

Oka, S., Ishihara, T., 2009. Numerical study of aerodynamic characteristics of a square prism in a uniform flow. J. Wind Eng. Ind. Aerod. 97, 548–559.

PAREA-LiDAR, https://biz.kkc.co.jp/en/data/?id=laser.

Parente, A., Gorlé, C., Van Beeck, J., Benocci, C., 2011. Improved k–ε model and wall function formulation for the RANS simulation of ABL flows. J. Wind Eng. Ind. Aerod. 99 (4), 267–278.

Park, S., Fernando, H., Yoon, S., 2014. Simulation of flow and turbulence in the Phoenix area using a modified urbanized mesoscale model. Meteorol. Appl. 21 (4), 948–962.

Philips, D., Rossi, R., Iaccarino, G., 2013. Large-eddy simulation of passive scalar dispersion in a uniform urban-like canopy. J. Fluid Mech. 723, 404–428.

Qi, Y., Ishihara, T., 2018. Numerical study of turbulent flow fields around of a row of trees and an isolated building by using modified k-ε model and LES model. J. Wind Eng. Ind. Aerod. 177, 293–305.

Qian, G.W., Ishihara, T., 2019. Numerical study of wind turbine wakes over escarpments by a modified delayed detached eddy simulation. J. Wind Eng. Ind. Aerod. 191, 41–53.

Rodi, W., 1997. Comparison of LES and RANS calculations of the flow around bluff bodies. J. Wind Eng. Ind. Aerod. 69, 55–75.

Schatzmann, M., Olesen, H., Franke, J., 2010. Cost 732 Model Evaluation Case Studies: Approach and Results Cost Action 732 Quality Assurance and Improvement of Microscale Meteorological Models.

Simiu, E., Scanlan, R.H., 1996. Wind Effects on Structures: Fundamentals and Applications to Design.

Smagorinsky, J., 1963. General circulation experiments with the primitive equations: I. The basic experiment. Mon. Weather Rev. 91 (3), 99–164.

Sutherland, I.E., Hodgman, G.W., 1974. Reentrant polygon clipping. Commun. ACM 17 (1), 32–42.

Tucker, P.G., Mosquera, A., 2001. Introduction to Grid and Mesh Generation for CFD.

Varquez, A.C.G., Nakayoshi, M., Kanda, M., 2015. The effects of highly detailed urban roughness parameters on a sea-breeze numerical simulation. Boundary-Layer Meteorol. 154 (3), 449–469.

Xian, X., Tao, W., Qingwei, S., Weimin, Z., 2002. Field and wind-tunnel studies of aerodynamic roughness length. Boundary-Layer Meteorol. 104 (1), 151–163.

Yang, Q.S., Zhang, J., 2009. Simulation of horizontally homogeneous atmosphere boundary layer based on k-e variant models combined with modified wall functions. In: The Seventh Asia-Pacific Conference on Wind Engineering. Taipei, Taiwan.

Yang, B., Raupach, M.R., Shaw, R.H., PawU, K.T., Morse, A.P., 2006. Large-eddy simulation of turbulent flow across a forest edge. Part I: flow statistics. Boundary-Layer Meteorol. 120 (3), 377–412.

Yoshie, R., Mochida, A., Tominaga, Y., Kataoka, H., Harimoto, K., Nozu, T., Shirasawa, T., 2007. Cooperative project for CFD prediction of pedestrian wind environment in the Architectural Institute of Japan. J. Wind Eng. Ind. Aerod. 95 (9), 1551–1578.

Yoshie, R., Jiang, G., Shirasawa, T., Chung, J., 2011. CFD simulations of gas dispersion around high-rise building in non-isothermal boundary layer. J. Wind Eng. Ind. Aerod. 99 (4), 279–288.

ZENRIN, https://www.zenrin.co.jp/product/category/gis/basemap/zmaptown/index.html.